Fabrication and Characterization of Flexible Electrowetting Microlens Array and Magnetically Actuated Lens with Tunable-Focus

By Kari L. Van Grinsven

A dissertation submitted in partial fulfillment of

the requirements for the degree of

Doctor of Philosophy

(Electrical and Computer Engineering)

at the

UNIVERSITY OF WISCONSIN-MADISON

2019

Date of final oral examination: 8/9/2019

The dissertation is approved by the following members of the Final Oral Committee:

Hongrui Jiang, Professor, Electrical and Computer Engineering
Yu Hen Hu, Professor, Electrical and Computer Engineering
Luke Mawst, Professor, Electrical and Computer Engineering
Zongfu Yu, Associate Professor, Electrical and Computer Engineering
Peter Adamczyk, Assistant Professor, Mechanical Engineering

Abstract

The first sections of this report focus on flexible electrowetting on dielectric (EWOD) microlens array sheets. Since EWOD is a fast, well-established actuation method, it is used for a variety of applications ranging from microfluidics to electrowetting displays to electrowetting lenses. We therefore seek to develop a robust, scalable fabrication method for the realization of a EWOD microlens array on a flexible polydimethylsiloxane (PDMS) substrate, since a flexible substrate extends the range of possible applications of our system. We fabricated a 5 × 5 array of individually controlled electrowetting cells to manipulate silicone oil droplets via EWOD. The fabrication process utilized exclusively flexible materials to improve the robustness of the overall device and processing methods were adapted to accommodate the particular challenges posed by flexible materials. Simulation of the EWOD devices was conducted using ANSYS Fluent and showed the change in contact angle in response to voltage applied. Fabricated devices were also tested, with actuation of the oil droplet observed with up to 100 V (RMS) AC applied across underlying electrodes. We demonstrated fabrication of a fully flexible array and verified actuation to center droplets over the electrodes.

This work on a flexible EWOD microlens array was then expanded and revised with a new fabrication method to improve robustness of the device. The extended work also conducted full, optical characterizations of the resulting lenses and lens system. We fabricated a fully-flexible, focus-tunable microlens array on a sheet and demonstrated its imaging capabilities. Each liquid lens of the array is individually tunable via EWOD actuation and is situated on a PDMS substrate, which allows the lens array to operate as a reconfigurable optical system. In particular, we observed a significant increase in the field of view (FOV) of the system to 40.4° by wrapping it on a cylindrical surface as compared to the FOV of 21.5° obtained by the array on

a planer surface. We also characterized the liquid lenses of the system, observing a range of focus length from 20.2 mm to 9.2 mm as increased voltage was applied to each EWOD lens. A Shack–Hartmann wavefront sensor (SHWS) was used to measure the wavefront of the lens as it was actuated, and the aberrations of the lens were assessed by reporting the Zernike coefficients of the wavefronts.

The final part of this work focuses on another kind of liquid lens, this one magnetically actuated. Here, instead of fabricating an array of microlenses, we focus our attention to a single, large (diameter equal to 15 mm) liquid lens. The lens is composed of two liquid chambers separated by a PDMS membrane, one filled with silicone oil and the other with water. The membrane deforms symmetrically in response to the Lorentz Force and is capable of achieving focal lengths from -111 mm to -305 mm when operating in the divergent regime and from 146 mm to 272 mm when operating in the convergent regime. We also characterized the aberration of the lens via a SHWS and observed changes in the shape of the wavefront produced by the lens as a function of voltage applied.

Acknowledgments

I would like to express my sincere thanks to my advisor Professor Hongrui Jiang for all his advice and guidance throughout the course of my research

I would also like to thank the rest of my committee: Dr. Peter Adamczyk, Dr. Yu Hen Hu, Dr. Luke Mawst, and Dr. Zongfu Yu for their time and efforts.

It has been true honor to work with my current and former labmates. Much of this work would have been impossible without their encouragement and insight. I would like to thank Dr. Alireza Oushtiani, Dr. Aditi Kanhere, Dr. Chi-Chieh Huang, Dr. Yen-Sheng Lu, Dr. Yousuf Al-Moallem, Dr. Jae-Jun Kim, Dr. Mohammad Moghimi, Dr. Xiudong Wu, Dr. Yinggang Huang, Dr. Xi Zhang, Dr. Hewei Liu, Dr. Xuezhen (George) Huang, and Dr. Hao Bian, as well as Jayer Fernandes, and Yong Ho (Eric) Kwon. Aditi and Jayer deserve particular mention for their unending patience in letting me bounce ideas off of them, or simply work through problems aloud with them. We spent countless hours together and they always helped me to keep not only research but also life and all its nuances in perspective.

My gratitude to the staff at WCAM (now the Nanoscale Fabrication Center) and SML (now the Soft Materials Characterization Laboratory) for all their hard work keeping tools and facilities up and running, and especially to Dr. Mike Efremov for his technical assistance in developing new processes on the Parylene coat, and to Quinn Leonard and Hal Gilles in the cleanroom for their help in developing and troubleshooting processing steps.

And of course, infinite thanks go to my family, whose guidance and advice has kept me grounded throughout the long road of graduate school. Thanks to my brother, Joseph, for always being there cheer me up with a hug or distract me with silliness when I needed it most. And a special thank you to my parents, Gene and Linda Van Grinsven, both electrical engineers

themselves. Thank you to my Dad, who saw my talent and interest in science when I was young and would have never dreamed of discouraging it. Instead, he nurtured it by teaching me math well above my grade level when I got bored with what I was taught in school as a young child, asking me to help him solve problems in his basement workshop, giving my brother and I lessons on 'How a Car Works' during long drives. Thank you Dad, for the countless hours you spent with me on the phone and in person talking through the technical difficulties of that week's fabrication and measurement work. And thank you to my Mom, who understood what it was like to sit in classrooms where we felt vastly outnumbered by our male colleagues and talked me through it, and who, when she was in college, was so determined and so in love with engineering that she chose to change schools rather than change majors. Your example has been most inspirational of all. Thank you for always reminding me I belonged in this field, and that I belonged at this level of study. I might not have made it through without you. I am forever grateful.

Table of Contents

Table of Figures

1. Introduction

1.1 Tunable-focus liquid lenses

Liquid lenses have been well established as viable solutions to enable tunable focal lengths for imaging, which has lead to increases in versatility of imaging systems. Liquid lenses are particularly valuable in systems of small form factor. Size is increasingly a factor in today's world, as optical systems continue to be miniaturized to meet increasing demands for mobile and unobtrusive imaging capabilities. Tunable lenses operate by either changing the refractive index of the lens or by changing the curvature of the lens in order to induce a change in the focal length. They usually utilize two liquids of different indices of refraction, the curved interface between them defining the lens. There are a large variety of actuation methods that have been demonstrated for liquid lenses, including fluidic pressure [1–3], liquid crystal [4,5], hydrogel [6,7], thermal [8,9], magnetic [10,11], dielectrophoretic [12,13], and electrowetting [14–17].

Depending on the design of the lens and the actuation method in question, a tunable focus liquid lens can be diverging, converging, or move between both. A lens is said to be converging if when parallel light rays pass through the lens they bend, or refract, inwards, towards one another. For an ideal lens they will eventually converge into a single point, and the distance between the lens and this location is known as the focal length of the lens. Such a lens is also often called a convex lens (in the simplest case a plano-covex lens), because a traditional, solid lens made of glass will have to have a convex shape in order for refraction to lead parallel rays to converge after passing through it, since glass has a higher index of refraction then air. A lens is said to be diverging if when parallel light rays pass through the lens they refract outwards, away from one another. Since such a lens will never converge to a point, the focal length of a diverging lens is defined as negative. If we look at the diverging light rays which result from the

parallel beam being passed through the lens and trace them backwards to the opposite side of the lens, these virtual rays will converge at a location, and the distance between this location and the lens is the focal length of the divergent lens (Here, the focal length necessarily negative, since we are on the other side of the lens then in the converging case). Such a lens is often called a concave lens, (in the simplest case a plano-concave lens) because a traditional, solid lens made of glass will have to have a concave shape in order for refraction to lead parallel rays to diverge after passing through it.

Unlike conventional solid lenses which typically have only 2 interfaces (at the air/glass boundary on both sides of the lens), liquid lenses have at least 3 or more interfaces. This is because liquids must be held in some kind of container, all be it an optically transparent one. The first interface will often be some sort of solid substrate, then the first liquid, then the second immiscible liquid of different index of refraction, and then finally some sort of cap to seal the system. In this simple case, it is the shape of the liquid with the higher index of refraction which dictates the kind of lens formed. For example, if we have a system of water and oil, oil will have the higher index of refraction, so if the shape of the interface when moving from oil to water is concave, then the lens is divergent. If that same interface is convex, then the lens is a convergent lens. Because of this, an oil droplet on a planer substrate submerged in water will always form a convergent lens, while a water droplet on a planer substrate submerged in oil will always form a divergent lens.

This increase in the number of interfaces has the side affect of increasing the amount of light reflected at these interfaces. The reflectance at an interface for light of normal incidence can be described by the equation

$$R = \left|\frac{n_1 - n_2}{n_1 + n_2}\right|^2 \tag{1.1}$$

where R is the reflectance, and n_1 and n_2 are the two different indices of refraction on each side of the interface. In the case of a interface between air (n=1) and standard glass (n=1.5), this gives a reflectance of approximately 4% at each interface. Since a simple, solid lens has 2 interfaces, the total percentage of light lost will be about 7.84%. To compare this to a liquid lens we will look at the case of a liquid lens described later in this report, in chapter 4. That lens has upwards of seven interfaces, but since the difference in the index of refraction between each of those interfaces is so much lower (n_{PDMS} = 1.43, n_{water} = 1.33, $n_{silicone\ oil}$ = 1.49, etc.) then between that of air and glass, the total percentage of reflected light from our liquid lens is only 10.63%, which is an increase of less than 3%.

1.1.1 Electrowetting on Dielectric (EWOD) actuators

Each actuation method has its own set of advantages and disadvantages; however, electrowetting on dielectric (EWOD) is particularly attractive thanks to its fast response times [18,19] and low power consumption. Additionally, since we aim to fabricate not just single devices, but an array of lenses, electrowetting actuation is especially well suited to forming an array of microlenses that can be actuated independent from on another because electrowetting avoids cross-talk between lenses (For instance, lenses in an array are easily insulated from one another electrically, but not easily insulated thermally).

While the work reported here focuses on optical lens applications of electrowetting actuators, EWOD actuation can be utilized by a wide variety of applications, ranging from a mechanism in microfluidic systems for cell sorting to a mechanism to turn ‘on’ and ‘off’ pixels in electrowetting color displays. For a more extensive discussion on the many possible applications of EWOD actuators, refer to section 3.1 of this report.

The easiest situation with which to demonstrate the mechanisms behind EWOD actuation is in the situation shown in Figure 1.1. A droplet of conductive liquid (often a diluted concentration of KCl in water) is placed on a substrate with a conductive electrode layer covered by a dielectric layer. Voltage is applied to the KCl saline by inserting the tip of a fine needle into the saline droplet and grounding the electrode beneath the dielectric layer. When 0V is applied the contact angle of the saline is determined by the surface tension, but with increasing voltage the attraction of opposite charges applied across the thin dielectric layer slowly overcomes the surface tension. As a result, the contact angle of the saline droplet decreases as voltage increases. This process if reversable, meaning that the droplet will relax back to a state with larger contact angle when the applied voltage is removed, though some degree of hysteresis is common.

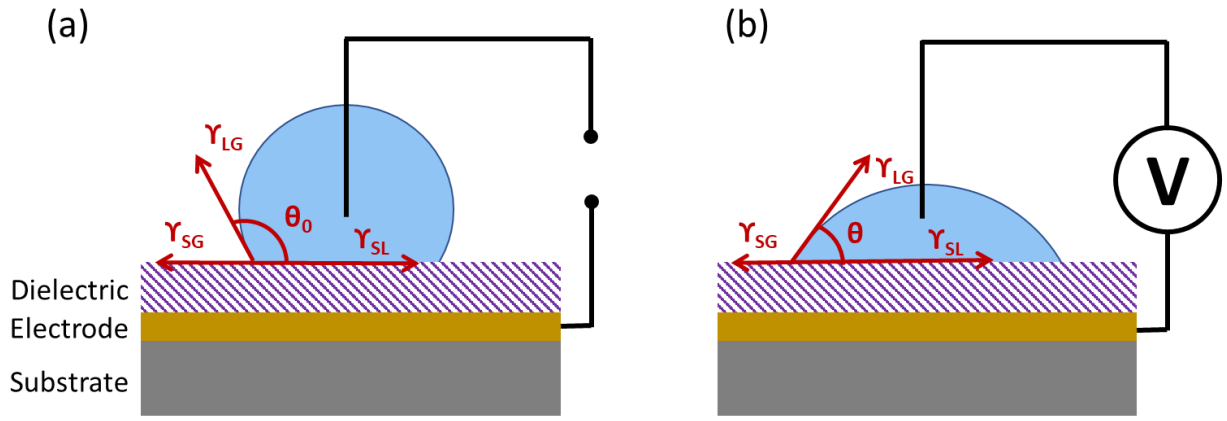

Figure 1.1. *Diagram of simplest electrowetting actuation, composed of a conductive liquid droplet on a dielectric layer which insulates it from the underlying electrode. The initial contact angle of the liquid is θ_0, after voltage is applied across liquid and dielectric layer the contact angle reducing to θ. [20]*

The change in contact angle of the saline droplet can be described using the Lippmann-Young equation

$$cos\,\theta\,(V) = cos\,\theta_0 + \frac{\varepsilon_0 \varepsilon_r}{2d\gamma_{LG}} V^2 \qquad (1.2)$$

where θ_0 is the initial contact angle of the saline, ε is the dielectric constant of the dielectric in question, d is the thickness of the dielectric, γ_{LG} is the surface tension between the saline and air (liquid and gas), and V is the voltage applied across the system. This means that in order to maximize the change in contact angle for a given change in voltage we want to use a thin insulator with high dielectric constant. Even still, EWOD system tend to require rather high driving voltages, though it is worth noting that in the idea DC case, the system consumes almost no power, since the EWOD system behaves as a capacitor.

Using EWOD to actuate a liquid lens means that the practical design needs to be modified from the simple example shown in Figure 1.1. First, instead of having a conductive liquid surround by air (an insulator), we surround the conductive liquid with an insulating oil. This has several advantages. Among them is preventing evaporation of our conductive liquid over time, and to provide density matching between the two liquids. This makes the lens more robust after the liquids have been sealed inside of the liquid lens chamber. And of course, in order to use the immiscible liquids as a lens we need to have an unobstructed optical path. This prohibits the use of an obstructing electrode or needle. Instead, we use a structure like the one shown in Figure 1.2. The needle is replaced with a transparent, indium tin oxide (ITO) electrode as the base substrate on which the saline droplet rests, while the sidewalls of a well-structure have an electrode covered with dielectric. This means that instead of the saline being attracted downwards towards the electrodes as in Figure 1.1, the saline is now naturally pinned at the corner boundary (repelled from the sidewalls of the well), but is attracted up the sidewalls as increasing voltage is applied.

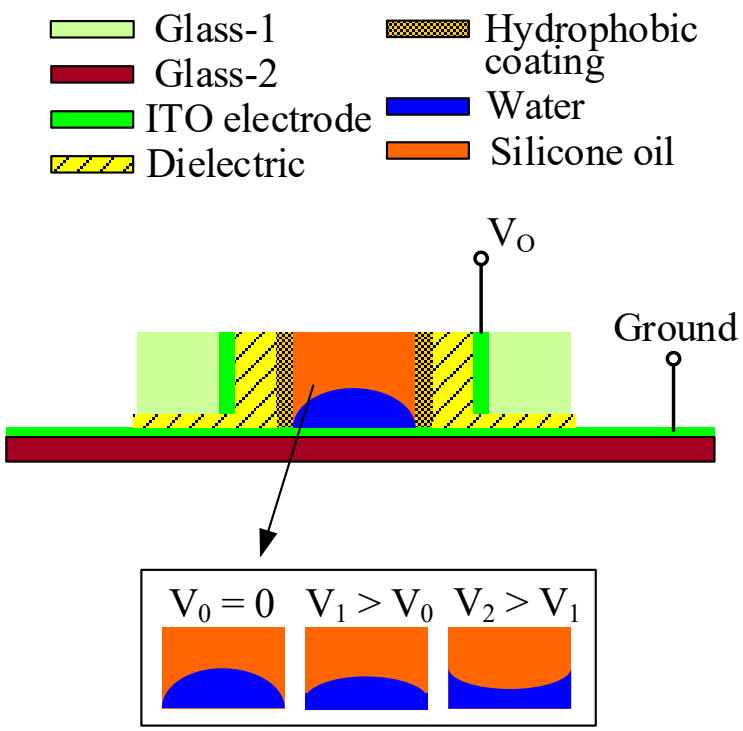

Figure 1.2. *Diagram of EWOD lens composed of water surrounded by silicone oil. As DC voltage is applied across the ITO substrate and the electrodes on the sidewall the attractive force begins to overcome the repellent surface energy of the hydrophobic walls and the water begins to move up the sidewalls. At a critical voltage the interface will be flat (radius of curvature equal to infinity) after which point the lens flips from concave to convex.*

Any lens produced by the design in Figure 1.2 forms a concave (diverging) lens in its rest state, because the index of refraction of silicone oil is greater than that of water/saline. If enough voltage is applied the lens can be flipped so that it becomes a convex (converging) lens. The dioptric power of the lens as a function applied voltage can be calculated be the following equation, which is closely related to Equation (1.2)

$$D(V) = D_0 + \frac{\varepsilon_r \varepsilon_0 (n_2 - n_1)}{2 d \gamma_{12}} V^2 \tag{1.3}$$

where D_0 is the initial power of the lens (determined by the amount of saline the lens container is filled with), ε is the dielectric constant of the insulating material, d is the thickness of the

insulator, n_1 and n_2 are the respective indices of refraction of water and oil, γ_{12} is the surface tension between the oil and water, and V is the applied voltage. This equation follows the same format as equation (1.2) because the power of a lens is directly related to its radius of curvature, which is determined by the contact angle of the water droplet. The point at which the dioptric power changes from negative to positive corresponds to the lens changing from concave to convex.

1.1.2 Magnetic Actuators

While we can imagine a system of liquids that directly responds and moves in response to changes in the magnetic field surrounding them the way that conductive water can respond the presence of an electrical potential, such a liquid would have to be a ferrofluid, none of which are optically transparent, and thus could not be used for optical purposes. So in the case of a magnetically actuated lens, the actuation mechanism is less direct then in the EWOD case.

To enable us to use any liquids of our choosing, we can instead introduce a flexible membrane in between the two liquids of our lens, and then attach to the membrane a magnetically responsive material outside of the optical path of the system that can be affected by the magnetic field to displace one of the liquids, causing the membrane to bulge and a lens to be formed. In order to maximize the variability of such a system we attach a coil of wire to the membrane. When we run current through the wire we can generate a force from the Lorentz force to displace the liquids and cause the membrane to bulge, forming a liquid lens. This actuation mechanism is described in more detail in chapter 5.

1.2 Microcamera systems

Any camera system requires at least three basic components: a lens, a detector and an aperture between the lens and the detector. Detectors can take a number of forms. Historically,

the primary detector was film—a sheet embedded with light reactive crystals that could later be developed and eventually enlarged. But in the present day most detectors are digital, with pixel counts on the order of megapixels, either made from CCD or CMOS sensor technology. There are also different kinds of lenses which can be used in a camera system. Here we will focus on microcamera systems and the potential kinds of lenses suited to them.

1.2.1 Pinhole cameras

The simplest (and oldest, dating back to the 1600s) kind of camera system is a pinhole camera. In this camera system the lens and the aperture have been combined into a single, simple pinhole. A pinhole camera works by severely restricting what kind of light from an object will be permitted through to the sensor plane. The small aperture (typically on the range of a 50-500 μm when being paired with a modern sensor) allow only light rays traveling in line with the aperture to reach the sensor, cutting off all other angles (and diminishing the amount of light with reaches the sensor in the process).

A pinhole camera has an infinite depth of field, but often suffers from a lack of sharpness, which can only be improved by decreasing the size of the aperature. This in turn further restricts the light which can reach the sensor and requires even longer exposure times. In this regard, it is not particular good for imaging objects in motion. A related drawback of a pinhole camera is its large f-number (f/#). The f-number of an optical system is

$$f/\# = \frac{f}{d} \tag{1.4}$$

where f is the focal length and d is the diameter of the aperture. For a pinhole camera the focal length is simply the distance to the sensor. The f/# of a lens affects the depth of field of the camera, and also the maximum possible resolution of a lens. The larger the f/# the lower the

contrast that will be observed at any particular resolution, thus and large f/# will lead to lower resolution then a smaller f/#. A typical pinhole camera has an f/# on the order of f/200.

1.2.2 Rigid lens cameras with small form factor

While the size of a lens was once limited by what a lensmaker could effectively handle and manipulate for precision grinding, modern technology means that while somewhat more expensive, small-diameter lenses of good quality can be produced. There is inherently, however, only one way to tune the focal length of a rigid lens, and that is to translate it via highly precise mechanical movements relative to the sensor. This is possible, but not always ideal. In cell phone cameras (perhaps the most ubiquitous in regards to cameras of small form factor), this mechanical movement has historically been provide by voice coil motors (VCMs). Voice coil motors have been around for almost a century, but still have drawbacks in regards to stroke hysteresis as well as size and relatively power requirements. But the most problematic of these drawbacks is that VCM designs cannot rule out the potential for the lens it moves to tilt or become decentered in the system, which can negatively impact image quality [21]. More recent cell-phone camera designs have utilized MEMS (microelectromechanical systems) linear actuators which are thinner and consume less power. They utilize a variety of designs such as electro-static comb drives or silicon flexures, but may be more prone to issues of durability and longevity [22,23].

1.2.3 Focus tunable lens cameras

The final kind of microcamera system then, is one that utilizes a focus-tunable lens. In this case, instead of needing to translate the position of the lens relative to the sensor, we can directly modulate the focal length of the lens. This eliminates the need for any precision mechanical movements. Additionally it should be noted that liquid lenses are particularly well

suited to applications at small form factor, since some of the well known issues with liquid lenses, namely vibration sensitivity and gravity effects, no longer become an issue at smaller sizes. This is because when a droplet becomes small enough the surface tension forces begins to dominate, minimizing potential distortions. A liquid microlens (water in air) of height up to 0.73 mm experiences no distortion due to gravity [24]. Since the liquid lenses in this work all utilize two density-matched liquids (water and silicon oil) we expect there to be little to no distortion due to gravity at a significantly larger radius of curvature, including the maximum 3 mm diameter of our electrowetting lenses.

Cameras which utilize a tunable focus lens are also able to sweep the focus of the over all camera system through a larger range of focal lengths at high rates of speed. Electrowetting lenses exhibit actuation times on the order of 50 ms [19], with any settling oscillations fully dissipated within 100 ms [18]. We expect our electromagnetically actuated lens to operate on an even more rapid time-scale, since the Lorentz force which drives the actuation engages the moment current starts to flow through the wire winding and we have used low-viscosity liquids on each side of our flexible membrane.

1.3 Lens characterization methods

1.3.1 Resolution targets

There are many different types of optical resolution targets which can be used to judge the quality of a camera system, however, the 1951 USAF resolution target, which consists of groups of horizontal and vertical bars, is the most common. Within a group, each bar is of an equal width to the gap between bars in that group, and the spacing between then decreases as you move closer to the center of the target (i.e. the number of line pairs per mm, lp/mm, increases as group and element number increases). This allows us to measure both horizontal and vertical

resolution simultaneously and all that is needed to compare lens quality to the diffraction limited case is the smallest resolvable element and the distance of the target to the lens.

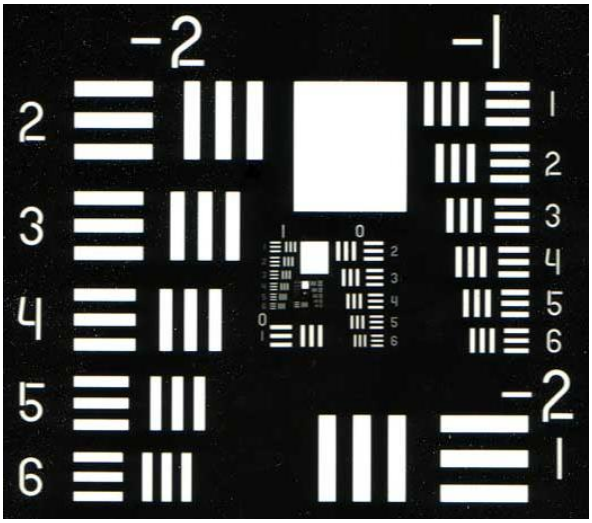

Figure 1.3. *1951 United States Air Force (USAF) resolution target*

1.3.2 Shack-Hartmann wavefront sensor

The Shack-Hartmann wavefront sensor uses a fixed, high density microlens array to analyze the shape of any wavefront that impinges on it. A plane wave will focus light into an even grid of points on the sensor, and a distorted wavefront will displace the focal point up/down or left/right depending on the average angle of the plane wave as it hits the microlens array. This displacement can then be measured and converted back to construct the shape of the original wavefront in software. The process and geometry involved are shown in Figure 1.4.

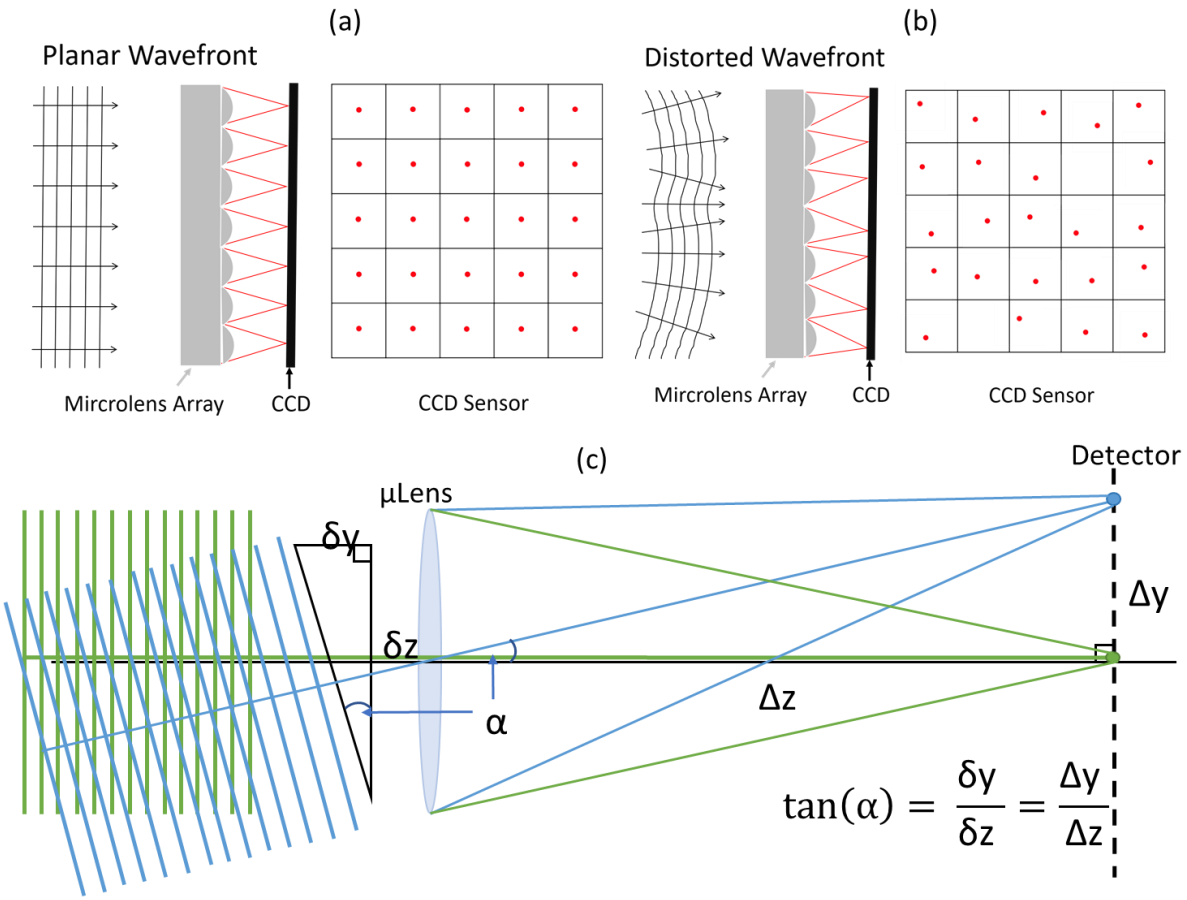

Figure 1.4. *Diagrams of the function of a Shack-Hartmann wavefront sensor.*

Once the wavefront shape has been reconstructed, the resulting shape can be fit with a set of Zernike function, which form a basis set. Individual Zernike coefficients are then related to various types of aberration often found in lenses, such as astigmatism or spherical aberration.

1.3.3 Modulation transfer function

The modulation transfer function (MTF) is function that characterizes the ability of an optical system to transfer contrast of an image at a given resolution. Since contrast generally decreases along with spatial resolution, it is useful to be able to describe the two aspects in relationship to one another. The MTF is defined as

$$MTF(\xi) = \frac{2}{\pi}(\phi - \cos\phi \sin\phi) \tag{1.5}$$

$$\phi = \arccos(\xi/\xi_c) \tag{1.6}$$

$$\xi_c = \frac{1}{\lambda\, f/\#} \tag{1.7}$$

where ξ is the spatial resolution, ξ_c is the cut-off frequency (the frequency where the MTF goes to zero), λ is the wavelength and f/# is the f-number of the system. Thus, we generally observe that systems with larger f-number generally have lower effective spatial resolution.

References

[1] Werber, A.; Zappe, H. Tunable microfluidic microlenses. *Appl. Opt.* **2005**, *44*, 3238–3245.

[2] Moran, P.M.; Dharmatilleke, S.; Khaw, A.H.; Tan, K.W.; Chan, M.L.; Rodriguez, I. Fluidic lenses with variable focal length. *Appl. Phys. Lett.* **2006**, *88*, 041120.

[3] Feng, G.-H.; Chou, Y.-C. Flexible meniscus/biconvex lens system with fluidic-controlled tunable-focus applications. *Appl. Opt*. **2009**, *48*, 3284–3290.

[4] Ren, H.; Fan, Y.-H.; Wu, S.-T. Liquid-crystal microlens arrays using patterned polymer networks. *Opt. Lett*. **2004**, *29*, 1608–1610.

[5] Ren, H.; Fox, D.W.; Wu, B.; Wu, S.-T. Liquid crystal lens with large focal length tunability and low operating voltage. *Opt. Express* **2007**, *15*, 11328–11335.

[6] Aldalali, B.; Kanhere, A.; Fernandes, J.; Huang, C.C.; Jiang, H. Fabrication of polydimethylsiloxane microlenses utilizing hydrogel shrinkage and a single molding step. *Micromachines* **2014**, *5*, 275–288.

[7] Kanhere, A.; Lin, G.; Jiang, H. Remote Axial Tuning in Microscopy Utilizing Hydrogel-Driven Tunable Liquid Lens. *J. Microelectromec. Syst*. **2016**, *25*, 304–310.

[8] Zhang, W.; Zappe, H.; Seifert, A. Wafer-scale fabricated thermo-pneumatically tunable microlenses. *Light Sci. Appl*. **2014**, *3*, e145.

[9] Ashtiani, A.O.; Jiang, H. Thermally actuated tunable liquid microlens with sub-second response time. *Appl. Phys. Lett*. **2013**, *103*, 111101.

[10] Lee, S.W.; Lee, S.S. Focal tunable liquid lens integrated with an electromagnetic actuator. *Appl. Phys. Lett*. **2007**, *90*, 2005–2008.

[11] Yu, H.; Zhou, G.; Chau, F.S.; Sinha, S.K. Tunable electromagnetically actuated liquid-filled lens. *Sensors Actuators, A Phys*. **2011**, *167*, 602–607.

[12] Almoallem, Y.D.; Jiang, H. Double-Sided Design of Electrodes Driving Tunable Dielectrophoretic Miniature Lens. *J. Microelectromec. Syst*. **2017**, *26*, 1122–1131.

[13] Xu, S.; Ren, H.; Wu, S.T. Dielectrophoretically tunable optofluidic devices. *J. Phys. D Appl. Phys*. **2013**, *46*, 483001.

[14] Berge, B. Liquid lens technology: Principle of electroweeting based lenses and applications to imaging. In Proceedings of the 18th IEEE International Conference on Micro Electro Mechanical Systems 2005 (MEMS 2005), Miami Beach, FL, USA, 30 January–3 February 2005; pp. 227–230.

[15] Krogmann, F.; Monch, W.; Zappe, H. A MEMS-based variable micro-lens system. *J. Opt. A Pure Appl. Opt.* **2006**, *8*, S330.

[16] Kuiper, S.; Hendriks, B.H.W. Variable-focus liquid lens for miniature cameras. *Appl. Phys. Lett*. **2004**, *85*, 1128–1130.

[17] Ousati Ashtiani, A.; Jiang, H. Design and fabrication of an electrohydrodynamically actuated microlens with areal density modulated electrodes. *J. Micromech. Microeng*. **2016**, *26*, 015004.

[18] Van Grinsven, K.L.; Ousati Ashtiani, A.; Jiang, H. Fabrication and Actuation of an Electrowetting Droplet Array on a Flexible Substrate. *Micromachines* **2017**, *8*, 334.

[19] Li, C.; Jiang, H. Electrowetting-driven variable-focus microlens on flexible surfaces. *Appl. Phys. Lett.* **2012**, *100*, 231105.

[20] Caputo, D.; de Cesare, G.; Vecchio, N.L.; Nascetti, A.; Parisi, E.; Scipinotti, R. Polydimethylsiloxane material as hydrophobic and insulating layer in electrowetting-on-dielectric systems. *Microelectronics Journal* vol. 45, no. 12, pp. 1684-1690, **2014.**

[21] Gutierrez, R.C.; Fossum, E.R.; Tang,T.K. Auto-focus technology. In Proceedings of the International Image Sensor Workshop, Ogunquit, ME, USA, 7-10 June 2007; pp. 20-25.

[22] Towfighia, S.; He, S.; Ben Mrad. R. A Low Voltage Electrostatic Micro Actuator for Large Out-of-Plane Displacement. In Proceedings of the ASME International Design Engineering Technical Conferences & Computers and Information in Engineering Conference, 17-20 August 2014, Buffalo, NY, USA; p. V004T09A015.

[23] Gutierrez, R.C.; Tang, T.K.; Calvet, R.; and Fossum, E.R. MEMS digital camera. In Proceedings of SPIE, vol. 6502, Digital Photography III, 20 February 2007; p. 65020K.

[24] Liu, Y.; Aldalali, B.; Jiang, H. Lateral tunable liquid microlenses for enhanced fluorescence emission in microfluidic channels. *J. Micromechanics Microengineering* **2012**, *22*.

2. Rigid EWOD lens containers embedded in flexible array

Since the basic electrowetting lens design discussed in section 1.1.1 is the most well-know and well-established for reliable focal length tuning of a liquid lens, we initially proposed to build many such rigid lens containers containing tunable-focus liquid lenses which would then be embedded or attached to a flexible substrate to create a flexible array of lenses.

2.1 Materials and Fabrication methods

Having previously familiarized ourselves with the behavior of electrowetting on dielectric, we turned our attention to the design and fabrication of the individual lenses to be utilized in our camera sheet. The liquid lens is formed by two immiscible liquids, conductive saline (a 1% KCl solution) and insulating oil, silicone oil. The basic device structure is composed of two pieces of glass which come together to form a well to hold the liquids for the lens (see Figure 2.1).

The device structure was made first by drilling a 1 mm diameter hole through a glass microscope slide using a high-grit, sintered diamond drill bit. Drilling introduced an unacceptably high degree of surface roughness to the sidewalls of the lens well. This was corrected by using an Su-8 reflow process. Su-8 microspray photoresist was applied to the drilled glass and then reflowed by heating to the glass transition temperature of the Su-8. This yielded a smooth sidewall surface for deposition. 300 nm of aluminum was sputtered onto the top and sidewalls of the device structure. This was followed by ~150 nm of sputtered SiO_2. Finally, the top structure was dip coated in Teflon to make the sidewall hydrophobic. The bottom piece of glass was sputtered with ITO, a transparent conductor, and then bonded with the top glass piece with adhesive to create the lens well. A schematic of this design is shown in Fig 2.1a-b and an image of the actual fabricated device can be seen in Figure 2.2.

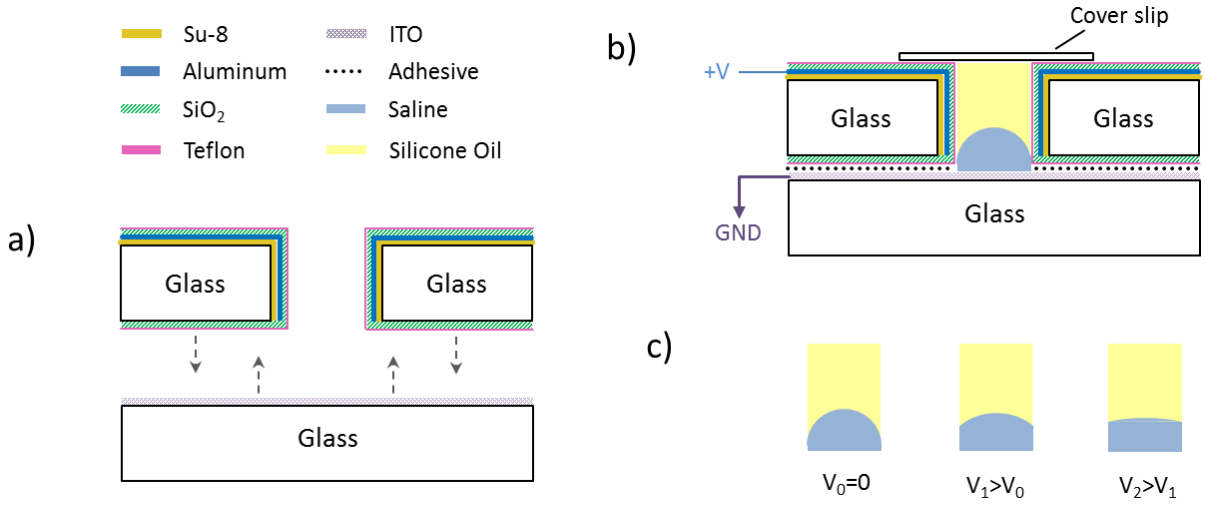

Figure 2.1. *a) Schematic of the two glass microscope slides used to form the lens well. b) Schematic of assembled device after the two pieces have been assembled. The lens is formed by the saline-oil interface, and voltage is applied across the device between Al on the top piece and the ITO grounding plane on the bottom. c) Illustration of the change in lens curvature as increasing voltage is applied across the device. This change in curvature corresponds to change in lens focal length.*

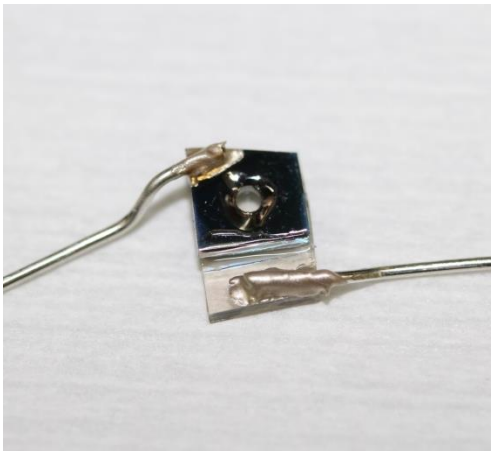

Figure 2.2. *Image of electrowetting lens structure (lens diameter = 1 mm) showing leads for applying potential.*

The contrast in surface energies at the interface of the hydrophilic sidewalls of the lens well and the hydrophilic glass of the base of the lens well causes the saline-oil boundary to

initially pin at the base of the well (see Figure 2.1b) when the device has been filled. The saline is grounded via the ITO grounding plane on the base piece of the well, which it is in direct contact with. Then, voltage is applied across it and the aluminum. This causes the saline to be attracted towards the sidewalls of the well which leads to a flattening of the lens. This flattening corresponds to a change in focal length of the lens. Increasing voltage increases the attractive force which further flattens the lens, as illustrated in Figure 2.1c. This affect will be shown experimentally in the next section.

2.2 Actuation results

After fabrication of the liquid lens wells was completed, they were manually filled with saline then silicone oil before being covered with a piece of cover glass. The lens was then moved to a stereoscope set up. This set up had first, on the stage of the stereoscope an optical object (a piece of transparency on which the UW ‘W’ had been printed in repeating pattern) followed by spacers to give several mm of height, followed by the lens itself. When the lens is viewed from the top by the stereoscope the virtual image produced by the lens can be brought into focus.

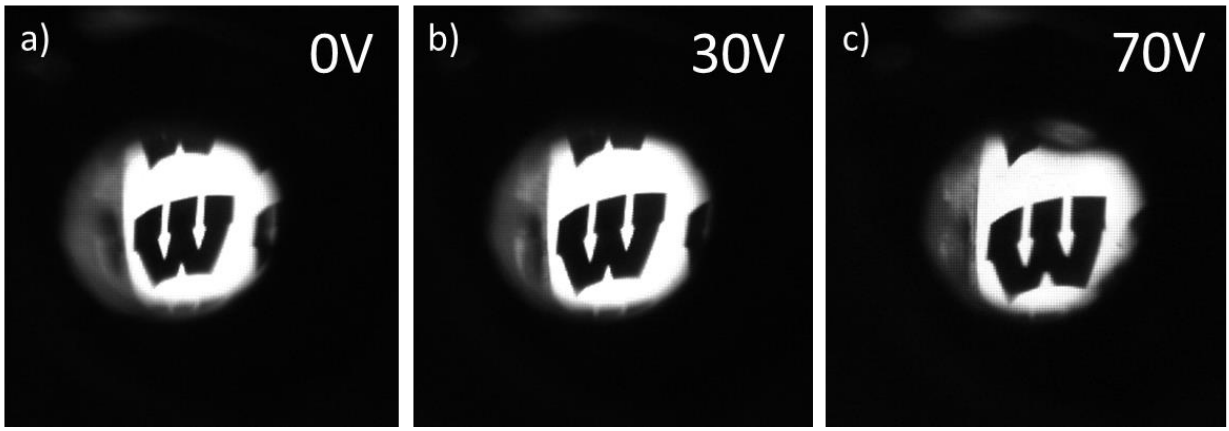

Figure 2.3. *The image produced by the electrowetting lens gradually magnifies with increasing voltage. This magnification corresponds to a change of focal length as the liquid lens flattens in response to applied voltage.*

While these rigid electrowetting lens containers were shown to function as tunable lenses (as in Figure 2.3), they were also prone to very high rates of breakdown and failure. These failures were almost certainly caused by defects in the dielectric induced by the inherent roughness induced by the action of physically drilling a whole through each microscope slide. Many attempts were made to reduce this roughness, both with HF dips and with Su-8 spray coating reflow, however, given the very thin dielectric layers that were all that was feasible via RF sputtering of SiO2 (due to low deposition rate), they were not effective enough. When a lens failed it either failed to actuate at all (i.e. broken circuit between electrode contact on top of glass to sidewall of structure) or a short occurred through the dielectric. This most often resulted in either the burning and thus discoloration of the ITO thin film, or the production of gaseous bubbles within the conductive liquid as the high voltage short occurred.

2.3 Flexible sheet design and simulation

We also modeled the mechanical properties and characteristics of the camera sheet as a whole in order to optimize the design of the array. This was done by using ANSYS to model the proposed geometry of the array of small islands for the cameras on a flexible substrate. Here, we have used PDMS for our flexible substrate and Su-8 for the square islands that sit atop it and contain our lenses. The small legs support the islands above the substrate were also modeled with PDSM. The substrate was then wrapped on different geometries to test flexibility (Figure 2.4).

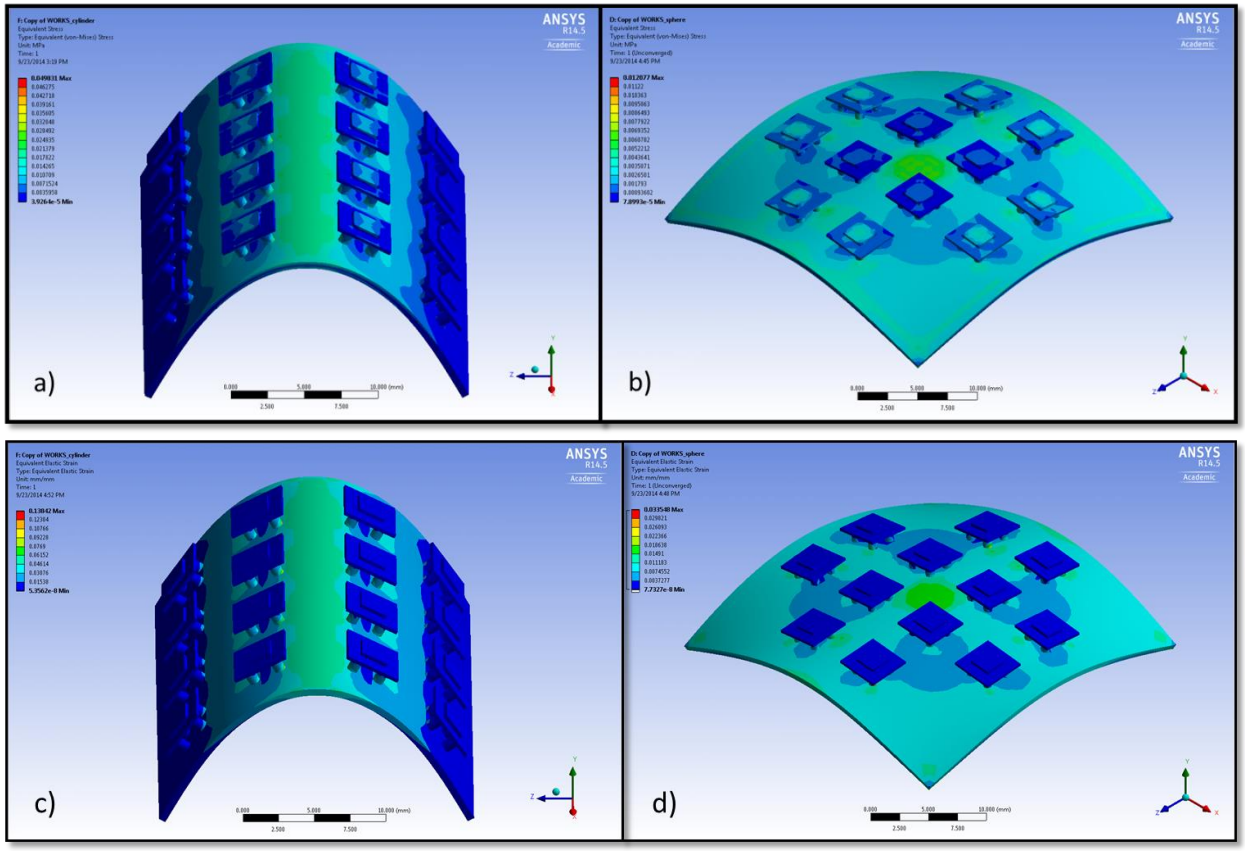

Figure 2.4. *ANSYS simulations of deformation of the camera array. The stress as the array is bent over* ***(a)*** *a cylindrical surface and* ***(b)*** *a spherical surface. The elastic strain as the array is bent around the same* ***(c)*** *cylinder and* ***(d)*** *sphere*

2.4 Discussion

Over time, the high failure rate of our rigid lenses combined with the inability for the lenses to be fabricated using a batch fabrication process (i.e. drilling wells through the glass must be done one well at a time, in a serial fashion) made it clear that a new approach was necessary in order to make an array of EWOD lenses possible. The work found in the following two chapters outlines the new approach we chose to utilize in order to achieve our goal of a flexible EWOD microlens array.

3. Flexible EWOD microlens array with dual-dielectric layer

3.1 Introduction

The use of microfluidic systems for precise manipulation and analysis of liquids has long been established as a crucial tool for a large array of fields, and biological processes such as cell sorting and counting in particular [1]. While microfluidic systems take advantage of a large array of actuation methods including pressure, capillary, pumps, and various electrokinetic mechanisms, few provide the degree of reconfigurability demonstrated by electrowetting on dielectric (EWOD) lab on chip systems. In such systems, transport of droplets does not require a physical, predefined microchannel but instead a droplet can be induced to move along a reconfigurable path in a plane by applying voltage potentials across underlying electrodes insulated from the liquid itself via a dielectric layer [2–5]. These electrowetting based systems have also been shown to perform a large variety of microfluidic tasks beyond mere transport, including droplet creation, merging/mixing of droplets, cutting/dividing of droplets, and liquid lens actuation [4,6]. More complicated systems which utilize EWOD actuation in combination with dielectrophoresis (another electrohydrodynamic actuation method) have been used for manipulating cell concentrations within fluid droplets [7]. However, none of these EWOD microfluidic systems has been extended to fabrication on a flexible substrate. Substrate flexibility allows for a wider range of applications for the system. For instance, it is well known that substrate flexibility is a regulatory parameter for certain kinds of cell growth [8]. Integration of cell growth, transport and measurement into a single system could therefore benefit from the use of a single flexible substrate for all functions.

Alternative situations where flexibility of the underlying substrate may prove useful is in electrowetting displays, which utilize EWOD to manipulate black or colored liquid droplets in

individual cells to act as pixels on a display by being actuated from on to off state by applied voltage. As interest grows in flexible and wearable electronics, flexible electrowetting displays may become useful [9]. Wearable microfluidic systems also benefit from use of electrowetting as actuation method, since electrowetting allows for simpler interconnects for modular wearable devices [10]. Finally, liquid lenses with focal lengths tunable via electrowetting or dielectrophoresis may prove particularly useful in applications such as soft contact lenses capable of correcting presbyopia. In addition, there are a number of examples of actuation of lenses on flexible surfaces [6,11], but combining these lenses into an array has not been deeply explored. An array of tunable lenses on a flexible substrate would allow for a reconfigurable imaging system. An array of individual electrowetting cells is also useful in the case of electrowetting optical switches [12,13].

All of these applications motivate us to derive a robust, scalable EWOD system fabricated on flexible substrates. The particular electrode design chosen focuses on the manipulation of an oil droplet in an aqueous solution to vary the surface area covered (i.e. contact angle) and center the oil droplet over the electrode; however, the fabrication method we provide here could be easily adapted to a large variety of other electrowetting applications by utilizing different electrode geometries, or aqueous liquids could be actuated on the same electrode structure using dielectrophoresis. In our configuration, the electrodes are laid out in a 5 × 5 array which form the basis for a 5 × 5 array of individual electrowetting cells once assembly is complete. Each electrowetting cell can be individually actuated via its own voltage control, and the entire array is fabricated on a single, flexible polydimethylsiloxane (PDMS) substrate.

3.2 Design considerations

Electrowetting lenses require an external centering mechanism to keep the liquid lens aligned along the optical axis. This centering mechanism is most often achieved by fabricating the underlying device and electrodes to be non-planar [14,15]. However, this significantly complicates the fabrication of the lens structure and introduces further difficulties when implemented into the flexible microlens array. Instead, we utilize our previously demonstrated electrode design to elegantly implement a continuous tuning and centering mechanism with a planar structure on a flexible substrate. Flexible, individual liquid microlenses have proven to be viable [16,11], and extending this flexibility to an array allows for a wider field of view and more extensive reconfigurable optical system, which makes the tunable microlens array suitable to a larger variety of applications, particularly novel form factor surveillance.

In our design, each electrowetting cell in the array is composed of areal density modulated electrodes (shown in Figure 3.1) which we previously demonstrated provided good electrowetting actuation [17], but which have now been patterned on a flexible PDMS substrate. The electrodes are insulated by a dielectric layer with a patterned hydrophobic region over the electrodes as well as a PDMS ring to create a well which contains the two immiscible liquids actuated by the electrowetting. A droplet of silicone oil, an insulator, is placed atop the underlying electrowetting electrodes and then surrounded by water which is conductive and serves as a floating electrode. As voltage is applied across the underlying areal density modulated electrodes, the liquids in the electrowetting cell will shift to minimize the potential energy of the system, since minimizing the potential energy is equivalent to maximizing the capacitance of the system according to Equation (3.1)

$$U = \frac{1}{2}\frac{q^2}{C}, \tag{3.1}$$

where U is the potential energy of the system, q is the charge, and C is the capacitance. By design, the potential energy can only be at a minimum when the silicone oil droplet is centered over the areal density modulated electrodes [17]. As the voltage across the underlying electrodes is increased, the conductive water, which functions as a floating electrode, is attracted down toward the electrodes to minimize the energy in the system by minimizing the distance between itself and the underlying electrodes. This means that the water will seek to cover more and more of the surface immediately over the electrodes as the voltage increases, effectively squeezing the silicone oil droplet which it surrounds.

By allowing the conductive liquid to act as a floating electrode instead of applying voltage directly across the conductive liquid, we choose to further enhance the robustness of the electrowetting application at the cost of increasing the voltage required to induce actuation. The robustness is further enhanced by applying an AC voltage to the system in order to reduce the chances of dielectric breakdown in the device.

Figure 3.1. *Schematic of areal density modulated electrodes used for electrowetting actuation. The interdigitated electrodes (+V) and counter electrodes (GND) cover an increasing percentage of the available area as the radius from center increases. This ensures that all forces on the oil droplet will be symmetric and that the droplet will be centered over the electrodes as voltage is applied.*

3.3 Materials and Fabrication methods

From start to finish, the conception and execution of the flexible substrate for our EWOD array required careful consideration of materials and fabrication method. This method is described visually in Figure 3.2. We chose PDMS as our flexible substrate because of its many attractive properties. PDMS is a biocompatible material with a degree of flexibility suitable for our purposes which grows increasingly robust with increasing thickness. This means that a relatively thin sheet of approximately 250 μm is strong enough to be easily handled and manipulated—an important characteristic for attaching the flexible array to any desired curvilinear surface.

For the micromachining process, it is necessary to make use of a carrier wafer of a 3-inch glass wafer (after clean room work has been completed, PDMS can simply be peeled off the wafer). PDMS was deposited on the carrier wafer via spin coating at 500 rpms for 30 s. The PDMS was then allowed to self-planarize on a level hot plate before being cured at 75 °C for 7 h. This process yielded a PDMS layer of approximately 250 μm with sufficient adhesion to underlying glass wafer to not cause any further processing difficulties during micromachining. There is, however, one key drawback to the choice of PDMS for our substrate. The low surface energy of PDMS means that metals exhibit very low adhesion to the substrate [11], and even when adhesion difficulties are overcome by applying a plasma treatment to the PDMS prior to metal deposition, the metal thin film remains highly susceptible to propagating spider-web cracking.

In order to overcome this difficulty, we chose to deposit Parylene C as an adhesion layer between PDMS and the copper electrodes of our devices. Parylene C is ideally suited to this task because it produces a conformal coat with outstanding adhesion to cured and untreated PDMS. It

additionally serves as a protective barrier for the PDMS in later processing of the substrate—PDMS is prone to swelling when exposed to water and other liquids which are standard to micromachining processes such as lithography, but Parylene C has a very low permeability to moisture. Additionally, when deposited in thin enough layers, Parylene C does not interfere with the flexibility of the substrate as a whole. We therefore deposited a 10 μm layer of Parylene C on our PDMS substrate and subsequently moved on to metal deposition.

Next, a copper thin film of 275 nm was deposited onto the PDMS and Parylene C substrate via magnetron sputtering. Deposition was conducted at the low power of 200 W in order to minimize the heating to the substrate which is inherent in the deposition process and has the potential to induce cracking in the copper thin film. Patterning of the copper was conducted using the standard photolithography processes. Positive photoresist (S1813) was exposed, developed, hard baked, and then used as a mask for the copper, which was wet etched in a commercial copper etchant (APS-100 copper etchant) diluted with DI water in a 4 to 1 ratio (DI water to etchant) at room temperature for 3 min.

After the photoresist was stripped and the wafer cleaned, a second layer of Parylene C was deposited over the patterned electrodes. This second conformal and pinhole free film of 2.5 μm of Parylene C served as the insulating, dielectric layer to prevent shorts from occurring in our electrowetting devices. This encapsulated the entire wafer in a strong dielectric material (dielectric constant of 3.10 at 1 kHz) with large breakdown voltage (5600 V/mil) [16] in order to ensure robust operation of our electrowetting devices. However, to gain access to the contact pads on the edges of the wafer, where external voltage will be applied to the electrowetting devices, a Parylene C etching step is required. A thick, positive photoresist (AZ P4620) was used to mask the whole wafer except the area directly over the contacting pads, and reactive ion

etching (RIE) was used to etch through the Parylene C. The wafer was etched using a 400 W RIE oxygen plasma etch for 4 min.

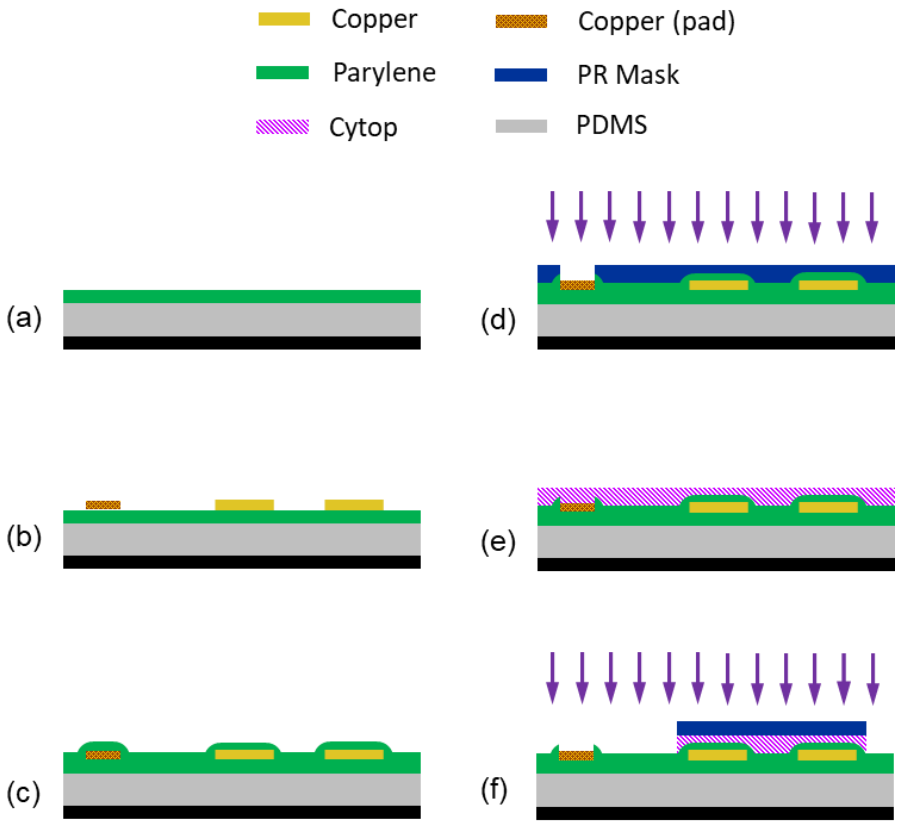

Figure 3.2. *Micromachining fabrication process of flexible electrowetting array.* ***(a)*** *250 µm of PDMS was spin coated onto a carrier wafer. After PDMS was cured a 10 µm layer of Parylene C was deposited as an adhesive layer;* ***(b)*** *275 nm of copper was deposited via magnetron sputtering and then patterned and wet etched into areal density modulated array electrodes along with traces and pads;* ***(c)*** *Another 2.5 µm of Parylene C was deposited over the whole wafer to act as a pinhole free dielectric layer;* ***(d)*** *The Parylene C insulator was etched in the region directly over pads for electrical contacts. A thick photoresist was patterned to act as a mask while Parylene C was etched used 400 W oxygen plasma;* ***(e)*** *1 µm of CYTOP was spin coated and cured to create a highly hydrophobic surface. The curing was done at a low temperature to minimize thermal strain to the flexible substrate;* ***(f)*** *CYTOP layer was pattered using a photoresist mask to protect the disk directly over the electrowetting electrodes. CYTOP was etched using 200 W oxygen plasma*

The final step in the micromachining process was to define a highly hydrophobic circular region immediately over the areal density modulated electrodes. To achieve this hydrophobic region, we used a 1 μm thin film of an amorphous fluoropolymer CYTOP (CTX-809SP2, a 9% solution by weight) on top of the Parylene C. This multilayer approach further reduces the chances of a short occurring in the device [18], but most importantly defines a hydrophobic region where the oil droplet can be initially placed. This is because the highly hydrophobic surface will prefer silicone oil over water, which should induce pinning at the boundary of the CYTOP disk. To achieve an array of properly patterned disks over our electrode arrays, the first step was to spin coat CYTOP at 4000 rpms. The CYTOP was then cured. Curing temperature was kept as low as feasible because of potential damage to the array from mismatched thermal expansion coefficients between PDMS and Parylene C. The wafer was transferred to an oven where it was prebaked at 50 °C for 1 h before the temperature was gradually increased to 110 °C and held for 6 h before being slowly allowed to cool back to room temperature. Standard curing procedures for CYTOP call for a baking temperature of at least 180 °C, however the maximum temperature of 110 °C was chosen because it slightly exceeds the value of the glass transition temperature of CYTOP, which is 108 °C. Ensuring the temperature was above the glass transition temperature allowed for superior evaporation of solvents from the CYTOP film [19]. After curing, the CYTOP was patterned in a process similar to that used to pattern the Parylene C. Photoresist (S 1813) was used to mask the array of disks and then the CYTOP was etched in a low power oxygen plasma RIE (200 W), which has the additional advantage of acting as a surface treatment for exposed Parylene C to render it temporarily hydrophilic. The photoresist is then carefully stripped, thus completing micromachining.

The final step in assembling the array is to attach rings molded from PDMS to the area around each electrode array to form the well to hold the two immiscible liquids. This is done using uncured PDMS as an adhesive between the rings and flexible substrate and manually aligning the rings to the array under the microscope. Once this PDMS adhesive layer has been cured, the PDMS substrate can be carefully peeled off the carrier wafer, and the final step is to fill the wells with water (0.001 M KCl, 150 µS/cm) and silicone oil and then cover them to prevent liquid evaporation. A schematic cross section of a single electrowetting cell can be seen in Figure 3.3. Images of the fully assembled flexible array can be seen in Figure 3.4. At this point, the array is ready for voltages to be applied to pads so that electrowetting actuation can be observed.

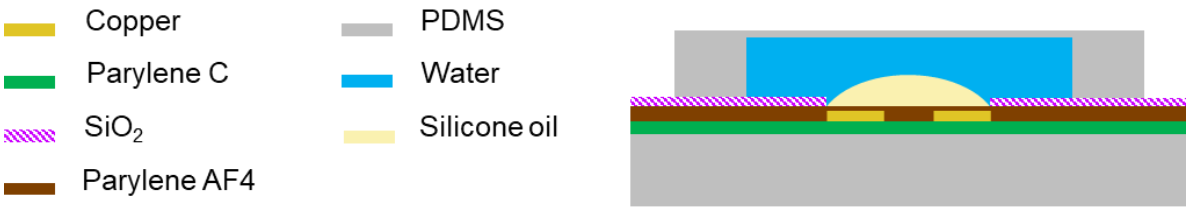

Figure 3.3. *Cross-section of a schematic of a single, fully assembled electrowetting cell. The well for containing the liquids for electrowetting was affixed using PDMS, and a silicone oil droplet was placed over the hydrophobic region of the flexible dielectric surface defined by the patterned CYTOP before being surrounded by water and sealed into the well.*

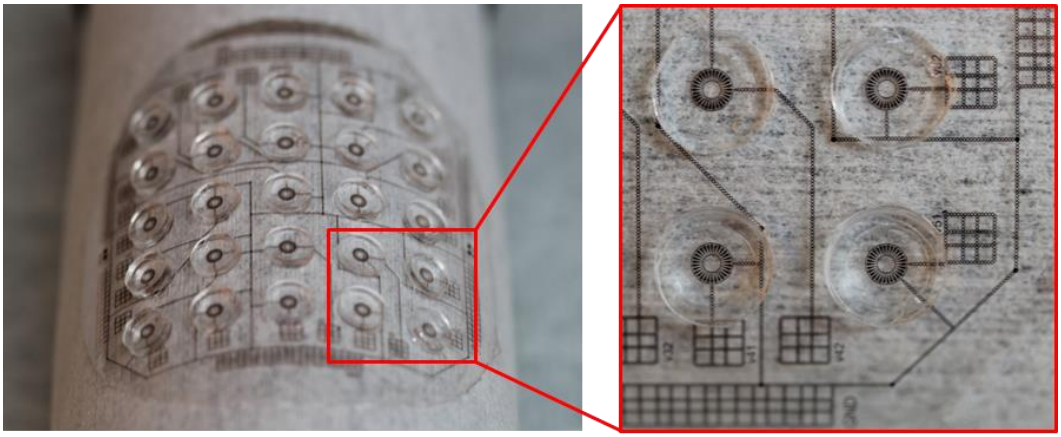

Figure 3.4. *Photographs of the fully assembled flexible electrowetting array on PDMS substrate showing: (**a**) the full 5 × 5 array wrapped on the surface of a cylinder and (**b**), a close up of one section of the array, showing individual electrowetting wells as well as traces and contact pads for applying voltage.*

3.4 Results

3.4.1 Simulations

Simulations were conducted in order to establish expected actuation of an individual electrowetting cell of the flexible array, as well as verify its mechanical and electrical feasibility. We chose to use ANSYS Fluent to gauge the change in shape of the oil droplet as voltage is applied to the electrowetting actuator. Since the devices were designed to be actuated via electrowetting on a two-layer dielectric the standard electrowetting equations can be applied to correlate voltage applied to the system to the expected contact angle. In the case of an insulator surrounded by a conductive liquid as in our design that equation can be expressed by Equation (4) [20]

$$\cos\theta = \cos\theta_0 - \frac{\varepsilon_0 \varepsilon_r}{2d\gamma} V^2 \tag{4}$$

where θ_0 is the initial contact angle of the insulator with external voltage applied, ε_r is the relative permittivity of the dielectric material, ε_0 is the permittivity of free space, d is the thickness of the dielectric layer, γ is the interfacial surface tension of the two liquids, V is the voltage applied to the system, and θ is the resulting contact angle of the insulating liquid.

In our case, the conductive liquid is not intrinsically grounded, but instead allowed to function as a floating electrode. This means we expect to have to apply twice the value of the voltage specified in Equation (4) in order to see the same change in contact angle, θ. Additionally, since our dielectric layer is in fact composed of two separate dielectrics (Parylene C and CYTOP) we can calculate an effective value of ε_r/d. Since the dielectrics are of constant thickness and one atop the other they can be considered to be in series so that we can write

$$\frac{\varepsilon_r}{d} = \frac{\varepsilon_1}{d_1} + \frac{\varepsilon_2}{d_2} \tag{5}$$

where ε_1 and ε_2 are the relative permittivities of each of the dielectric layers and d_1 and d_2 are their respective thicknesses.

Because of the highly hydrophobic nature of the CYTOP disk over the areal density modulated electrodes, any oil droplet of reasonable size should spread to cover the whole hydrophobic region to minimize the energy of the system. For the purpose of our simulation, we chose a silicone oil volume of 0.89865 μL. For this volume the initial contact angle of oil correlates to 40°. We chose as an area of interest contact angles between this initial, resting state value and 90°. From Equation (4) we see that this range corresponds to a voltage range of 0 to 71.56 V.

We set up ANSYS Fluent to run a multiphase model, which allows us to track the interface of two, user defined, immiscible liquids—in our case water and silicone oil with a viscosity of 20 cSt. We specified appropriate densities and viscosities for the liquids in the

simulation set up. We also specified the interfacial surface tension coefficient as 24.34 dyn/cm [21]. The geometry of our system was imported to ANSYS and regions of different wettability were identified. The wettability of the CYTOP surface directly over the electrodes of our system was set to vary according to Equation (4), and thus changed from one simulation to the next. The substrate, sidewalls, and lid of our chamber—which corresponded to the edges of our domain in ANSYS—were defined as constantly hydrophilic (contact angle of water equal to 10°), and the regions inside of the CYTOP disk but not directly above an electrode were defined as constantly hydrophobic (contact angle of water equal to 140°).

Simulation solutions were calculated using a non-iterative time step advancing method within the ANSYS software. In order to reduce simulation times, the size of each time step was allowed to vary in accordance with the global courant number of simulation (set to 2.0). To ensure the most accurate interface of our two immiscible liquids, geometric reconstruction was used to evaluate the interface at each step. Each simulation began at the natural state of the system (contact angle of silicone oil equal to 40°) and then saw an abrupt change of surface energies, leading to a corresponding change in contact angle as the simulation progresses. Each simulation was allowed to run for 100 ms in order to allow damping of transient oscillates as the oil droplet moves. The results of these simulations can be seen in Figure 3.5.

Under close observation, we note a scalloping affect at the edges of the water-silicone oil-CYTOP interface. This is to be expected, since it corresponds to the boundaries of our interdigitated electrodes. The silicone oil directly over the electrodes is squeezed strongly, causing the overall actuation, but in the spaces between electrodes the surface is still highly hydrophobic. This means that the surface prefers the silicone oil to the surrounding liquid and the

local contact angle of the silicone oil is less. We also observe that all simulations appeared to have reached a steady state position by the completion of the 100 ms of calculation.

Simulations were also conducted to test the mechanical and electrical integrity of the electrowetting array design. ANSYS was used to create a static structural simulation of a single cell of the array in order to get a measure of the stress (von Mises, equivalent) which results when the substrate is wrapped around a cylinder with a radius of 30 mm (as in Figure 3.4). The simulation model was constructed to replicate the dimensions of the fabricated device and used the values of Young's modulus and Poisson's ratio found in Table 3.1. The results of this simulation, which show the only significant stress occurring within the copper electrodes, can be seen in Figure 3.6a. A maximum value of 46.304 MPa is returned for the simulation, with a stress generally at or below 40 MPa for large or crucial regions of the electrode, all of which are below the fracture strength for copper.

However, the stress on the copper could still be reduced further. If the flexible PDMS rings used to form the wells to contain the liquids of our electrowetting droplets were instead converted to a solid sheet with disks of open space centered around each droplet the neutral axis of the overall sheet would be shifted closer to the level of the copper traces, reducing the stress on them. This 'sheet of wells' would be fabricated via molding PDMS to be 500 μm thick with an additional 50 μm cap across the entire surface to seal the liquids into the well. The result of the ANSYS simulation of the stress for this revised geometry is shown in Figure 3.7, and return a maximum value of 10.477 MPa, which is less then a quarter of the value reached in the simulation of the flexible substrate without a sheet of wells. Future revisions of the flexible microlens array should utilize this design.

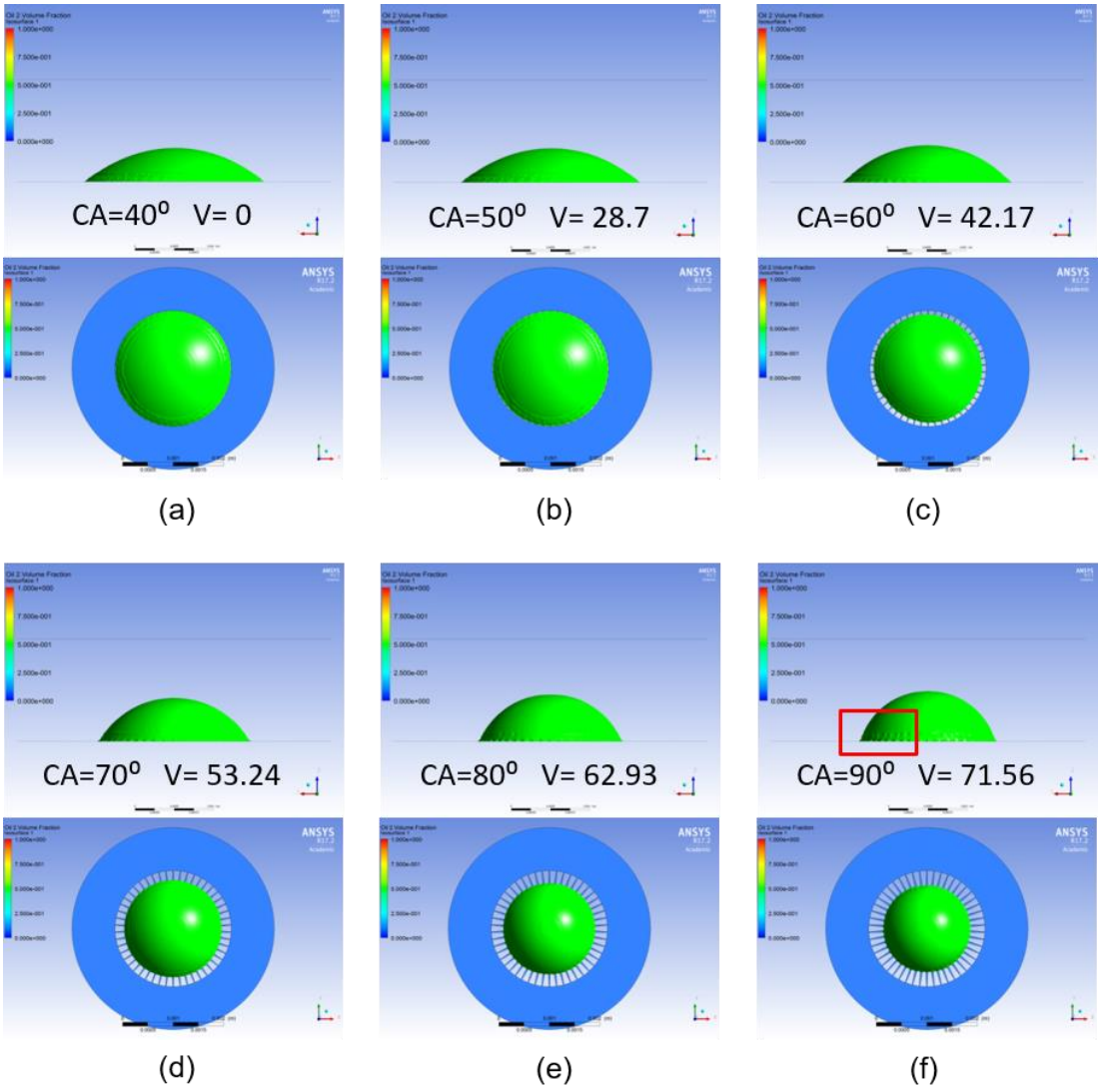

Figure 3.5. *Computational results of ANSYS Fluent simulation of silicone oil droplet surrounded by water under different levels of electrowetting actuation. The underlying electrode structure is shown in blue, the surface of the interface between water and oil is shown in green. Scalloping effect at interface is highlighted by red square. (**a**) The initial state of the fluidics system showing both top and profile view. The 40° contact angle of the oil is equivalent to no externally applied voltage; (**b**) The contact angle changes to 50° at 28.7 V after 100 ms elapsed simulation time; (**c**) the contact angle changes to 60° at 42.17 V after 100 ms; (**d**) the contact angle changes to 70° at 53.24 V after 100 ms; (**e**) the contact angle changes to 80° at 62.93 V after 100 ms; (**f**) the contact angle changes to 90° at 71.56 V after 100 ms.*

Finally, an electrostatic simulation was conducted in ANSYS Maxwell to determine the electrical potential on top of the insulators. Voltage was applied across the electrodes and counter-electrodes at 100 V DC, so that the simulation shows a snapshot of the 100 V AC square wave which is applied to the fabricated devices. The results in Figure 3.6b confirm that the voltage is uniform over the electrode areas.

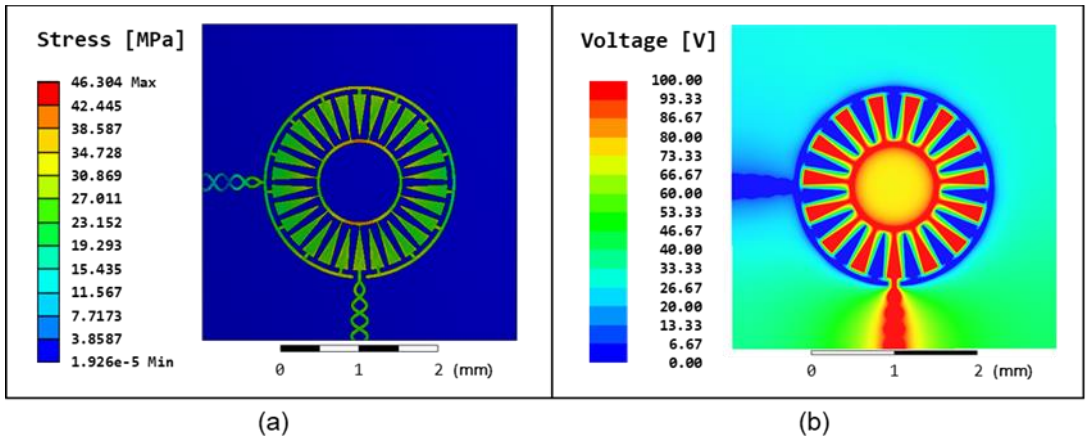

Figure 3.6. *(**a**) Static structural ANSYS simulation results of von Mises equivalent stress in a single electrowetting cell which has been wrapped around a cylinder of radius equal to 30 mm. Maximum stress is observed in the copper electrodes, but at levels well below the fracture point of copper; (**b**) ANSYS Maxwell electrostatic simulation of region on top of Parylene C and CYTOP insulators, where one set of interdigitated electrodes is ground, and the other set has had 100 V applied.*

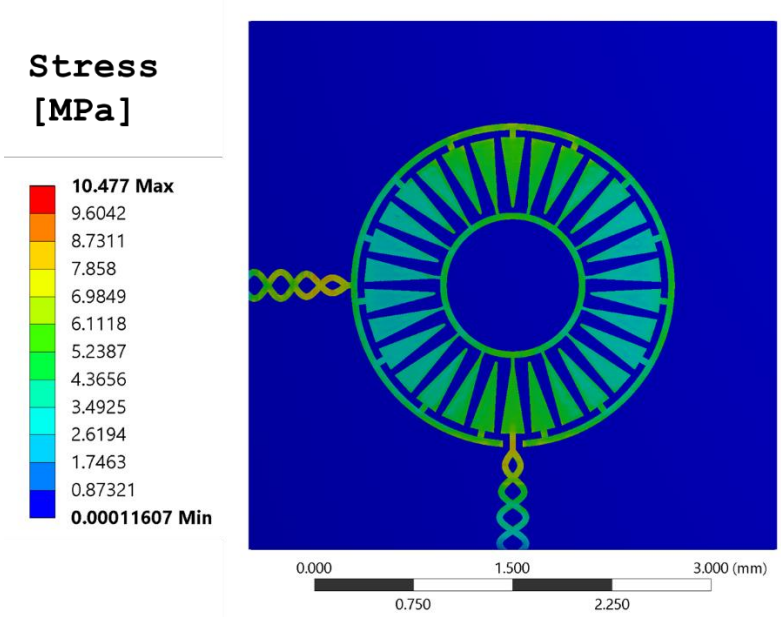

Figure 3.7. *Static structural ANSYS simulation results of von Mises equivalent stress in a single electrowetting cell which has been wrapped around a cylinder of radius equal to 30 mm, where the geometry of the simulation has been revised to include the presence of a well-sheet on top of the flexible substrate. The addition of this second layer greatly reduced the stress on the copper transmission lines form 46 MPa to 10 MPa, thus greatly improving the robustness of the design.*

Table 3.1. Values used in static structural ANSYS simulation to determine von Mises equivalent stress.

Material	Young's Modulus (MPa)	Poisson's Ratio
Copper	1.1×10^5	0.343
CYTOP	1500	0.42
Parylene C	2758	0.4
PDMS	0.5	0.48

3.4.2 Experimental results

Once we completed fabrication of our flexible array of electrowetting cells, we continued on to evaluate observable actuation when voltage was applied to the underlying pair of

electrodes. In order to ensure a good electrical contact with the exposed pads at the edges of our flexible substrate, we used conductive silver epoxy to affix wires and more easily apply voltage this way, without fear of damaging the electrical pads via probing. The flexible substrate was laid across an optically transparent, planar support and then place under the microscope. This allowed us to observe the silicone oil–water interface with good clarity.

As expected, we observed that the oil droplet was squeezed inwards as increasing voltage was applied to the system, because the voltage change attracts the water downwards and inwards to minimize the capacitance of the system. The applied voltage was chosen as an AC square wave with a frequency of 10 kHz, and the resulting actuation can be seen in Figure 3.8 (all voltages measured as RMS values). It is worthy of note that while the initial placement of the oil droplet over the electrodes was significantly asymmetric, the oil droplet is manipulated into an increasingly circularly symmetric shape as applied voltage is increased. This is as expected for our areal density array design. To minimize the capacitance of the system, the oil droplet will center itself over the electrodes as voltage is applied.

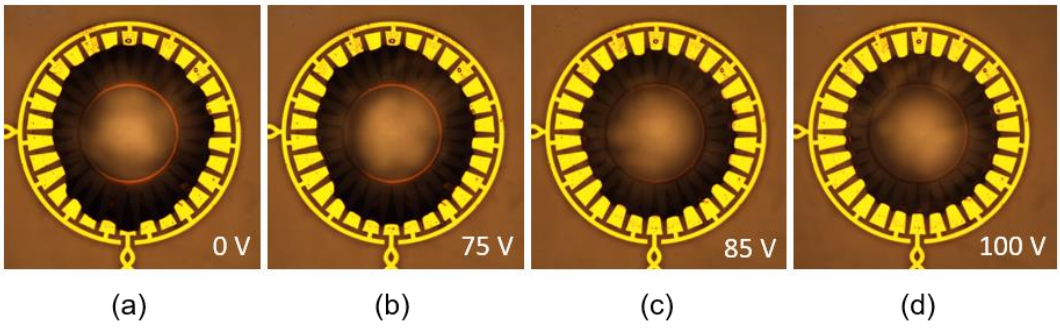

Figure 3.8. *Top view of the silicone oil droplet surrounded by water over electrowetting electrodes. Images were taken via microscope under 5x magnification as voltage (10 kHz, AC square wave) was applied to the system. (**a**) Initial position of the oil droplet, no voltage applied; (**b**) the oil droplet begins to be squeezed by surrounding water at 75 V (RMS); (**c**) droplet when 85 V (RMS) is applied; (**d**) droplet when 100V (RMS) is applied.*

Next, basic imaging capabilities of the lenses were tested under the microscope. A uniform array of simple stars was chosen to act as an object. The liquid lens was placed above the object plane by a few millimeters and the microscope was focused on the resulting image generated by the lens. The focus adjustment of the microscope was then locked and voltage was applied to the lens. The radius of curvature of the liquid lens decreased in response to the increase in applied voltage, which resulted in the defocusing of the image as the focal length of the liquid lens decreased. The progress of this defocusing can be seen in Figure 3.9.

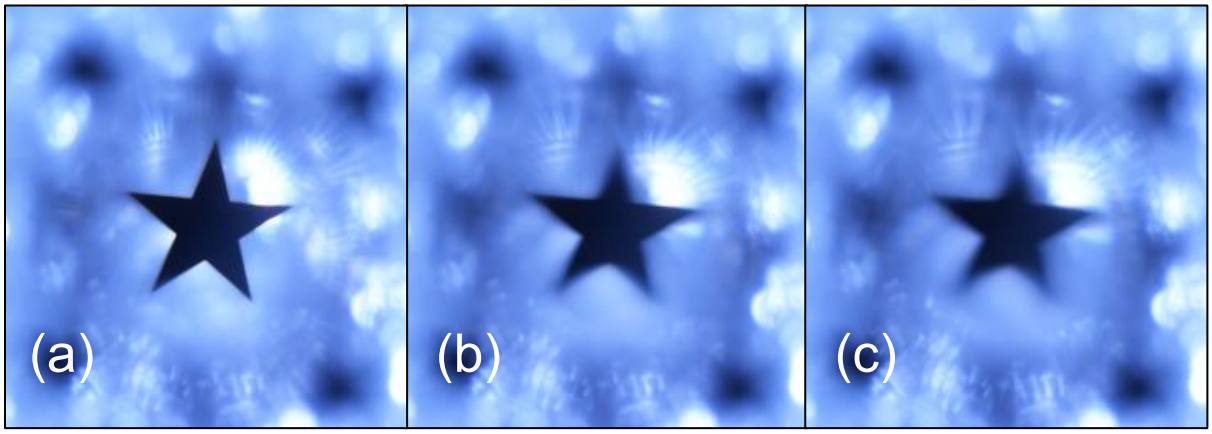

Figure 3.9. *Lens tuning demonstrated by image defocusing.* ***(a)*** *Image generated by the lens (a star) is initially focused at 0V.* ***(b)*** *75V AC square wave is applied across the electrode and the image begins to defocus.* ***(c)*** *Image further defocuses when 100V AC square wave applied.*

3.5 Discussion

We have demonstrated our fabricated EWOD array is capable of actuation, and that the electrode design does induce a centering of the oil droplet, as expected. Further, we note that the area covered by the oil droplet in our experimental results decreases as increasing voltage is applied. This corresponds to an increase in the contact angle, just as was observed in our

simulation results. Therefore, this trend is consistent across simulation and experimental results. Experimental testing required somewhat higher applied voltages then were required to induce actuation than our simulation results may have led us to believe. This discrepancy can be attributed to a number of factors. One possibility is that imperfections in the dielectric layers, particularly in the CYTOP layer since the fluoropolymer is applied via spin coating. These imperfections may effectively lower the relative permittivity of the CYTOP and thus increasing the voltage required to effect the same actuation. Another possible source of this increased voltage requirement may be charge entrapment in the CYTOP layer [22,23], effectively shielding some of the applied voltage.

We have also shown the feasibility of fabricating an electrowetting array composed exclusively of flexible materials, allowing it to operate while curved on any curvilinear surface. Copper traces designed with flexibility in mind also improve the robustness of flexibility in our design. Robustness of the array was further improved because the conductive liquid in the liquid well for each electrowetting actuator is allowed to float instead of being physically tied to ground of the system, which reduces the chances of electrical shorts. Simulation results demonstrated the effectiveness of symmetric actuation of a droplet of silicone oil to change its contact angle as external voltage is applied to electrodes. In simulation, contact angles ranging from 40º to 90º where observed, corresponding with voltages from 0 V to 71.56 V. This same symmetrical squeezing of the oil droplet experiencing electrowetting actuation was observed when fabricated samples were tested. These validate the possibility of future work in applying the basic material and fabrication design to more targeted applications, such as cell culturing and electrowetting lab on a chip applications.

In the next chapter we will pursue the use of a similar array for electrowetting microlens array applications. This work will involve characterizing the optical properties of the silicone oil droplet in water and assessment of aberrations. Work will also be done to reduce the driving voltage by decreasing dielectric thickness.

References

[1] Shields, C.W., IV; Reyes, C.D.; López, G.P. Microfluidic cell sorting: A review of the advances in the separation of cells from debulking to rare cell isolation. *Lab Chip* **2015**, *15*, 1230–1249, doi:10.1039/C4LC01246A.

[2] Pollack, M.G.; Shenderov, A.D.; Fair, R.B. Electrowetting-based actuation of droplets for integrated microfluidics. *Lab Chip* **2002**, *2*, 96–101, doi:10.1039/b110474h.

[3] Paik, P.; Pamula, V.K.; Pollack, M.G.; Fair, R.B. Electrowetting-based droplet mixers for microfluidic systems. *Lab Chip* **2003**, *3*, 28–33, doi:10.1039/b210825a.

[4] Cho, S.K.; Moon, H.; Kim, C. Creating, Transporting, Cutting, and Merging Liquid Droplets by Electrowetting-Based Actuation for Digital Microfluidic Circuits. *J. Microelectromech. Syst.* **2003**, *12*, 70–80, doi:10.1109/JMEMS.2002.807467.

[5] Jones, T.B.; Fowler, J.D.; Chang, Y.S.; Kim, C.J. Frequency-based relationship of electrowetting and dielectrophoretic liquid microactuation. *Langmuir* **2003**, *19*, 7646–7651, doi:10.1021/la0347511.

[6] Li, C.; Jiang, H. Electrowetting-driven variable-focus microlens on flexible surfaces. *Appl. Phys. Lett.* **2012**, *100*, doi:10.1063/1.4726038.

[7] Fan, S.; Huang, P.; Wang, T.; Peng, Y. Cross-scale electric manipulations of cells and droplets by frequency-modulated dielectrophoresis and electrowetting. *Lab Chip* **2008**, *8*, 1325–1331, doi:10.1039/b803204a.

[8] Wang, H.; Dembo, M.; Wang, Y. Substrate flexibility regulates growth and apoptosis of normal but not transformed cells. *Am. J. Physiol. Cell Physiol.* **2000**, *279*, 1345–1350.

[9] Steckl, A.J.; You, H.; Kim, D. Flexible electrowetting and electrowetting on flexible substrates. *Proc. SPIE* **2011**, *7956*, 1–6, doi:10.1117/12.871021.

[10] Fan, S.; Yang, H.; Hsu, W. Droplet-on-a-wristband : Chip-to-chip digital microfluidic interfaces between replaceable and flexible electrowetting modules. *Lab Chip* **2011**, *11*, 343–347, doi:10.1039/c0lc00178c.

[11] Lu, Y.S.; Tu, H.; Xu, Y.; Jiang, H. Tunable dielectric liquid lens on flexible substrate. *Appl. Phys. Lett.* **2013**, *103*, 261113, doi:10.1063/1.4858616.

[12] Murade, C.U.; Oh, J.M.; van den Ende, D.; Mugele, F. Electrowetting driven optical switch and tunable aperture. *Opt. Express* **2011**, *19*, 15525–15531, doi:10.1364/OE.19.015525.

[13] Ren, H.; Xu, S.; Ren, D.; Wu, S.-T. Novel optical switch with a reconfigurable dielectric liquid droplet. *Opt. Express* **2011**, *19*, 1985–1990, doi:10.1364/OE.19.001985.

[14] Kuiper, S.; Hendriks, B.H.W. Variable-focus liquid lens for miniature cameras. *Appl. Phys. Lett.*, **2004**, *85, no. 7*, 1128–1130.

[15] Krogmann, F.; Monch, W.; Zappe, H. A MEMS-based variable micro-lens system. *J. Opt. A: Pure Appl. Opt.*, **2006***, 8, no. 7*, S330–S336.

[16] Li, C.; Jiang, H. Fabrication and characterization of flexible electrowetting on dielectrics (EWOD) microlens," *Micromachines*, **2014**, *5, no. 3,* 432–441.

[17] Ashtiani, A.O.; Jiang, H. Design and fabrication of an electrohydrodynamically actuated microlens with areal density modulated electrodes. J. Micromech. Microeng. 2016, 26, 15004, doi:10.1088/0960-1317/26/1/015004.

[18] Schultz, A.; Chevalliot, S.; Kuiper, S.; Heikenfeld, J. Detailed analysis of defect reduction in electrowetting dielectrics through a two-layer "barrier" approach. *Thin Solid Films* **2013**, *534*, 348–355, doi:10.1016/j.tsf.2013.03.008.

[19] Asiri, H. Fabrication of Surface Plasmon Biosensors in CYTOP; University of Ottawa: Ottawa, ON, Canada, 2012.

[20] Liu, C.; Park, J.; Choi, J. A planar lens based on the electrowetting of two immiscible liquids. *J. Micromech. Microeng*. **2008**, *18*, doi:10.1088/0960-1317/18/3/035023.

[21] Than, P.; Preziosi, L.; Joseph, D.D.; Arney, M. Measurement of Interfacial Tension between Immiscible Liquids with the Spinning Rod Tensiometer. *J. Colloid Interface Sci.* **1988**, *124*, 552–559.

[22] Khodayari, M.; Carballo, J.; Crane, N.B. A material system for reliable low voltage anodic electrowetting. *Mater. Lett.* **2012**, *69*, 96–99, doi:10.1016/j.matlet.2011.11.060.

[23] Berry, S.; Kedzierski, J.; Abedian, B. Irreversible Electrowetting on Thin Fluropolymer Films. *Langmuir* **2007**, *23*, 12429–12435, doi:10.1021/la7017743.

4. Flexible EWOD microlens sheet for increased FOV

4.1 Introduction

While liquid microlenses were typically fabricated on rigid structures, there has been significant work in recent years to construct tunable liquid lenses on flexible substrates [1-4]. Similarly, there has been a variety of research on tunable microlens arrays [5-10]. However, the vast majority of such arrays have been either on rigid substrates or have shared actuation between lenses, meaning the focal length of one lens in the array cannot be tuned independently from its neighbor. Finally, almost none of these microlens array seek to image far-field scenes.

By seeking to create an array of electrowetting lenses on a flexible substrate we endeavor to achieve a highly reconfigurable imaging platform for visible wavelengths, capable of providing a wide field of view (FOV) when wrapped on a convex surface. This is done by stitching the individual images from the lenses in the array together into a single image, and the extent of the increase in FOV will be determined by the radius of curvature of the underlying surface. It is only limited by the requirement that there is at least some overlap between each image formed by the array. The independent turning of each lens in the array may also allow for imaging with a greater depth of field. These capabilities in combination with the unobtrusive form factor of the microlens array could have particularly relevant applications in imaging for monitoring or surveillance purposes. Additionally, wrapping the flexible substrate on a concave surface would enable the array to also be utilized for 3D imaging. In order to achieve the high yield required to make use of an array in which the entire array is fabricated together and individual components cannot be exchanged, we made use of an areal density modulated electrode design that we previously reported [11], which simplified the fabrication process and improved yield.

4.2 Materials and Methods

4.2.1 Principles of Operation and Design

Our actuation mechanism makes use of an areal density modulated electrode design with which we previously demonstrated electrowetting on dielectric (EWOD) functionality. While previous work focused on characterizing a single EWOD lens on a rigid substrate [11], or on developing methods to fabricate EWOD devices on flexible substrates [12], in this work we demonstrated a completely functional tunable lens array utilizing EWOD, and also turned our attention to the imaging capabilities of an array of lenses, making improvements to the design and fabrication methods in the process. The areal-density-modulated electrode design used by each liquid lens in our array can be seen in Figure 4.1a. It shows a circular grouping of interdigitated electrodes across which we apply voltage. The dielectric in our EWOD lenses is a relatively new kind of Parylene, a fluorinated Parylene known as Parylene AF4, which is hydrophobic. We add a thin, hydrophilic layer of SiO_2 to the surface surrounding our interdigitated electrodes in order to define a rest state for the oil droplet and surrounding water that composes our lens. As seen in Figure 4.1b the silicone oil droplet (with a refractive index of 1.49) would naturally pin at the Parylene AF4/ SiO_2 boundary as its rest state, creating a convex lens. More detail on material choices and fabrication methods can be found in Section 2.2.

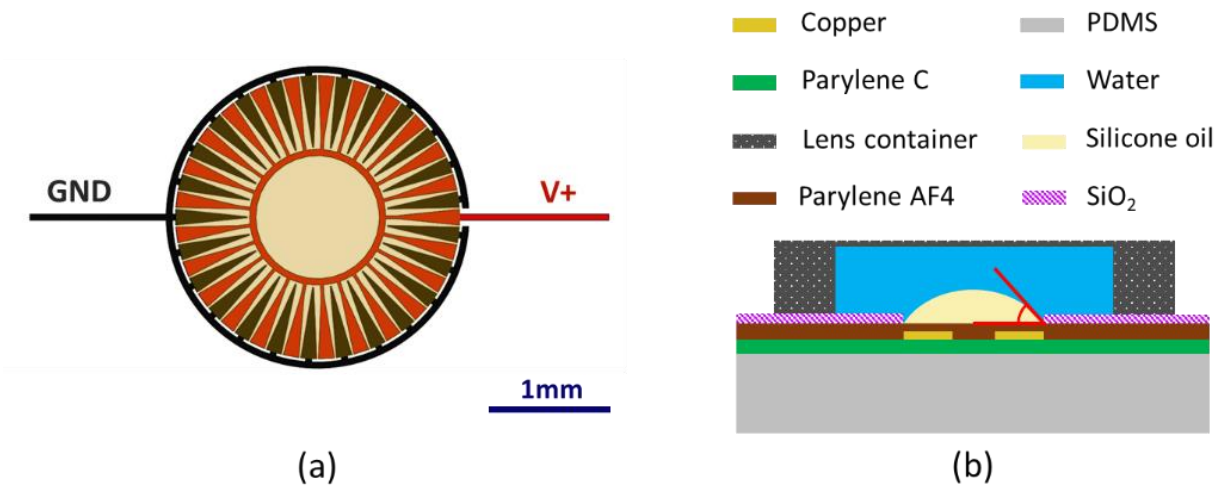

Figure 4.1. ***(a)*** *Top-down view of areal-density-modulated electrode design, where live and grounded electrodes are interdigitated. The pale, yellow disk over the center of the electrodes highlights the area where the surface is hydrophobic, where the oil will initially pin. As voltage is applied the oil droplet will be symmetrically squeezed by the water which surrounds it.* ***(b)*** *Cross-section of a schematic of a single, fully assembled electrowetting lens (not to scale). The well for containing the liquids for electrowetting was affixed with adhesive, and a silicone oil droplet was placed over the hydrophobic region of the flexible dielectric surface defined by the patterned SiO2 before being surrounded by water and sealed into the well. The red angle indicates the contact angle of the oil droplet.*

This design has several benefits, the first of which is that it allows analog focal length tuning of our lenses. As increasing voltage is applied across the underlying electrodes, the water of the lens—which acts as a third, floating electrode—is attracted down and in towards the electrodes, effectively squeezing the oil droplet. This squeezing means that the surface area covered by the oil droplet will decrease, and since the overall volume of oil must remain unchanged, the contact angle of the droplet (which forms a spherical cap) increases. This increase in contact angle corresponds to a decrease in the radius of curvature of the lens, effectively shortening the focal length of the system. The initial contact angle of the lens is

determined by the volume of its silicone oil droplet, and the contact angle of the lens as a function of the applied voltage is described by Equation (4.1):

$$\cos\theta(V) = \cos\theta_0 - \frac{\varepsilon_0\varepsilon_r}{2d\gamma}V^2 \tag{4.1}$$

where $\theta(V)$ is the contact angle of the oil droplet as a function of voltage, θ_0 is the initial contact angle (zero volts applied), ε_r is the relative permittivity of the dielectric layer, d is the thickness of the dielectric, γ is the interfacial surface tension of the oil and water, and V is the voltage applied. It should be noted that the sign of the equation is inverted compared to the standard electrowetting equation to account for the switching of the physical positions of the conductive liquid (here, water) and the insulating liquid (here, silicone oil) [13]. The superior film quality we achieved with Parylene AF4 (Yuan-Shin Materials Technology Corp., Kaohsiung, Taiwan) made it possible for us to significantly reduce the thickness of the dielectric layers, which reduced the required driving voltages.

The areal-density-modulated electrodes also serve as a self-centering mechanism for the lens, to ensure it remains centered on its optical axis. This effect is achieved by taking advantage of the fact that the system that composes our lenses will always attempt to minimize its potential energy. In order to do so, the capacitance of the system must be maximized, according to equation (4.2):

$$U = \frac{1}{2}\frac{q^2}{C} \tag{4.2}$$

where U is the potential energy, q is the stored charge, and C is the capacitance. Our electrodes have been designed such that the percentage of surface area where electrodes are present varies as a function of the radius from the central point of the electrodes. As seen in Figure 4.1a, at their outer edge (i.e., largest radial distance) the interdigitated electrodes cover the overwhelming fraction of the circumference, and as the radial distance decreases the electrodes

cover a decreasing fraction of surface area. In order for the system to maximize the capacitance, the water and oil will move so the water covers the largest possible area of the electrodes. This can only be achieved when it is centered over the electrodes, thus fixing the optical axis of the system [11]. This centering feature of the areal-density-modulated electrodes enables us to use a wholly planer design for our EWOD lens, which greatly simplifies the fabrication and improves the yield, the latter of which is crucial in the creation of an array of lenses.

4.2.2 Fabrication

In order to create our reconfigurable microlens array sheet we require the sheet to be suitably flexible while robust, and all materials must be chosen accordingly. The fabrication process, which needed to take into account the specific challenges inherent in working with such flexible materials, is shown in Figure 4.2. It began with the use of a carrier wafer (3 inch, mechanical grade silicon) that supported our polydimethylsiloxane (PDMS) substrate. The PDMS (SYLGARD 184, Dow, Midland, MI, USA) was deposited via spin coating at 500 rpms for 30 s. The edge bead which results from the spin coating process was removed manually, and then the PDMS was allowed to self-planarize on a level surface at room temperature before it was cured in a 75 °C oven for 7 h. This yielded a 250-µm PDMS layer, which is thin enough to give us a large degree of flexibility, but thick enough to be easily handled without damaging it. The wafer was then coated with a 2-µm layer of Parylene C in order to improve adhesion in the following sputtering steps, and to increase the stability of the flexible substrate.

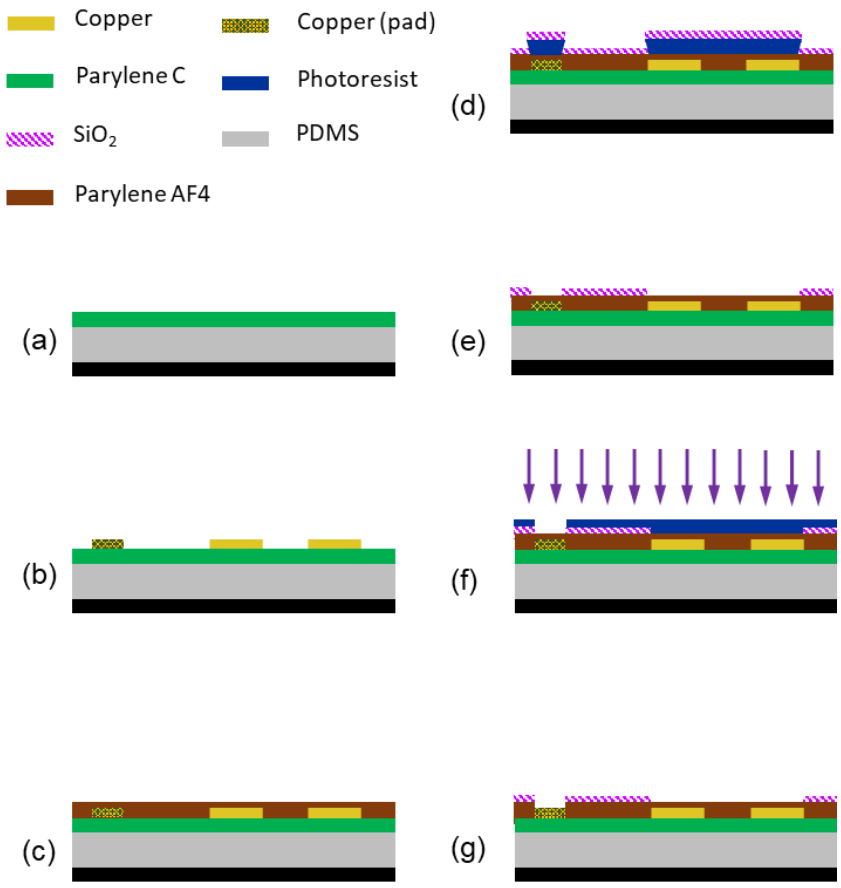

Figure 4.2. *Microfabrication process of a flexible electrowetting-based tunable lens array.* ***(a)*** *250 µm of PDMS is spin coated onto a carrier wafer. After PDMS is cured, a 2-µm layer of Parylene C is deposited as an adhesive layer.* ***(b)*** *275 nm of copper is deposited via magnetron sputtering and then patterned and wet-etched into areal density modulated array electrodes along with traces and pads.* ***(c)*** *800 nm of Parylene AF4 is deposited over the whole wafer to act as a pinhole free dielectric layer.* ***(d)*** *A lift-off type photoresist is patterned to cover contact pads and define the hydrophobic region immediately over the areal-density-modulated electrodes for each lens, then 100 nm of SiO2 is deposited via RF sputtering.* ***(e)*** *Lift-off of SiO2 was preformed via ultrasonic agitation in acetone.* ***(f)*** *Positive photoresist is patterned to protect all of wafer except areas over contact pads. A 200-W oxygen plasma is applied to etch Parylene AF4 down to copper contact pads to allow electrical contact to each device in the array.* ***(g)*** *Photoresist is stripped and a final cleaning of the wafer is completed.*

Next, a copper thin film of 275 nm was deposited onto the PDMS and Parylene C substrate via magnetron sputtering. The sputtering was performed at a low power of 200 W in order to reduce thermal expansion of the PDMS. After sputtering, the electrodes for each microlens in the array, their traces and contacting pads were all patterned via contact photolithography. Positive photoresist (S1813, MicroChem Corp., Westborough, MA, USA) was spin coated, exposed, developed, rinsed, and finally hard baked so that the photoresist could be used as a mask for wet etching of the copper. Wet etching was performed using a commercial copper etchant (APS-100 copper etchant, Transene, Danvers, MA, USA) diluted with DI water in a 4 to 1 ratio (DI water to etchant) and was done by submerging the wafer for 3 min at room temperature. The photoresist was then stripped, and the wafer rinsed prior to deposition of our dielectric layer.

We chose as our dielectric Parylene AF4 (sometimes referred to as Parylene HT), a fluorinated Parylene. While all variants of Parylene films have the attractive qualities of providing a conformal coating, being flexible, and providing good optical transparency in the visible range, Parylene AF4 has a number of unique characteristics that make it particularly attractive for use in our design. Many EWOD actuators have a prerequisite dielectric material, and then add another hydrophobic layer (usually an amorphous fluoropolymer such as Teflon). Nevertheless, since Parylene AF4 is inherently hydrophobic (contact angle of ~100°), an additional layer is not required. This allows for a decrease in the overall dielectric thickness, which reduces required driving voltages. Parylene AF4 also has superior penetration depths (up to 50:1 aspect ratio), which leads to superior film quality compared to the more common Parylene C [14]. The Parylene AF4 film was deposited using a vacuum vapor deposition polymerization (VDP) process in a LabTop 3000 Parylene coating system (Para Tech Coating,

Inc., Aliso Viejo, CA, USA) with Parylene AF4 dimer as the raw material for the system. As the Parylene moves through the coating system, the Parylene AF4 dimer is first vaporized, then broken down into a monomer in the pyrolysis chamber (heated to 705 °C) and finally polymerizes as a thin film onto our wafers in the deposition chamber at room temperature [15]. The resulting film was an 800 nm conformal coating of Parylene AF4 (see Figure 4.2c), which served as the insulating, dielectric layer to prevent shorts from occurring in our electrowetting devices. The wafer was coated in the dielectric material (dielectric constant of 2.25) with a robust breakdown voltage (216 kV/mm) [16]. The one drawback of Parylene AF4 is that, like most fluorinated materials it has a relatively low dielectric constant (which decreases the potential change in contact angle as seen in Equation (1)). However, the dramatic reduction in thickness allowed by the superior film quality more than compensates for this decrease.

After Parylene AF4 deposition, the entire wafer has been electrically insulated by the hydrophobic material. In order to help pin the liquids that our tunable liquid lenses will be composed from, we need the surface surrounding the underlying interdigitated electrodes to be hydrophilic, while the area directly over the electrodes remains hydrophobic. This circular disk with hydrophobic surface properties will define where our oil droplet resides and allows the surrounding water to naturally pin at the boundary (see Figure 4.1b). While all Parylene, including Parylene AF4, can be rendered temporarily hydrophilic via treatment with an oxygen plasma, we instead chose the more permanent solution of depositing a thin SiO_2 layer in the regions that require a hydrophilic surface property. The SiO_2 was deposited via radio-frequency (RF) sputtering in conjunction with a lift-off process to pattern, as seen in Figure 4.2d. This lift-process involved several steps. First, a negative lift-off photoresist (KL1604, KemLab, Inc., Woburn, MA, USA) was patterned via photolithography to protect the circular disks for our lens

placement as well as the areas over the contact pads. The wafer was then deposited with 100 nm of SiO_2 via RF sputtering at 140 W. After sputtering, the portions of film that had been deposited on the photoresist was removed by transferring the wafer to a beaker of acetone, which was then placed in an ultrasonic bath until the lift-off resist and the corresponding portions of the SiO_2 film was removed, as shown in Figure 4.2e.

Next, in order to gain access to the contact pads on the edges of the wafer where external voltage will be applied to the electrowetting devices, the Parylene AF4 insulating those areas needed to be etched. For this etch step, a thick positive photoresist (S1827, Shipley) was used to mask the whole wafer except the area directly over the contacting pads, and reactive ion etching (RIE) was used to etch through the Parylene AF4 to the copper below. The wafer was etched using a 200 W RIE oxygen plasma for 3 min. When the etch step was completed the wafer was then stripped of photoresist and given a final cleaning, which marked the end of cleanroom processing.

Final assembly was completed by affixing a lens chamber around each set of electrodes in the array in order to contain the liquids of the lens (see Figure 4.1b). For this, a 1.5-mm thick, flexible and transparent sheet composed of 50% ethylene vinyl acetate copolymer and 50% petroleum resin was cut into rings and then attached to the flexible substrate by placing the wafer on a 90 °C hotplate for 4 min. This melts the bottom layer of the rings and allows them to adhere to the flexible substrate. Finally, the substrate was carefully peeled from the carrier wafer, and the array of wells is ready to be filled with liquid to create the lenses. Each liquid lens was formed by manually placing a silicone oil droplet over the hydrophobic disk over the electrodes in the center of the well and then filling the surround area with water. The result, with water and oil pinned at the hydrophilic/hydrophobic interface can be seen in Figure 4.1b. After this, the

liquids are sealed inside the lens chamber by adhering an PET cover to the top of each ring. The only remaining step was to attach wires to the contact pads, so that voltage can be applied to induce electrowetting actuation. This was done using a conductive, double sided tape. Photographs of the fully assembled flexible sheet can be seen in Figure 4.3, which exhibit a 5 × 5 array of lenses with a center-to-center spacing of 10mm between each of the 25 lenses in the square grid array. This 10-mm pitch allows for the space required to align CMOS image sensors beneath each lens of the array. Since we designed this lens to image far field objects, this 10-mm pitch only requires that the substrate be not wrapped on a surface of so small a radius that there is no longer overlap between the field of view of each individual lens in the array. However, in order to do imaging of close-range objects the array would need to be redesigned at a smaller pitch. In this case, very small form factor CMOS sensors would need to be used, and most commercially available sensors of suitable compactness have a low pixel resolution (on the order of 257 × 257 pixel), whereas the sensor used for imaging in this paper has a sensor resolution of 2592 × 1944 pixels.

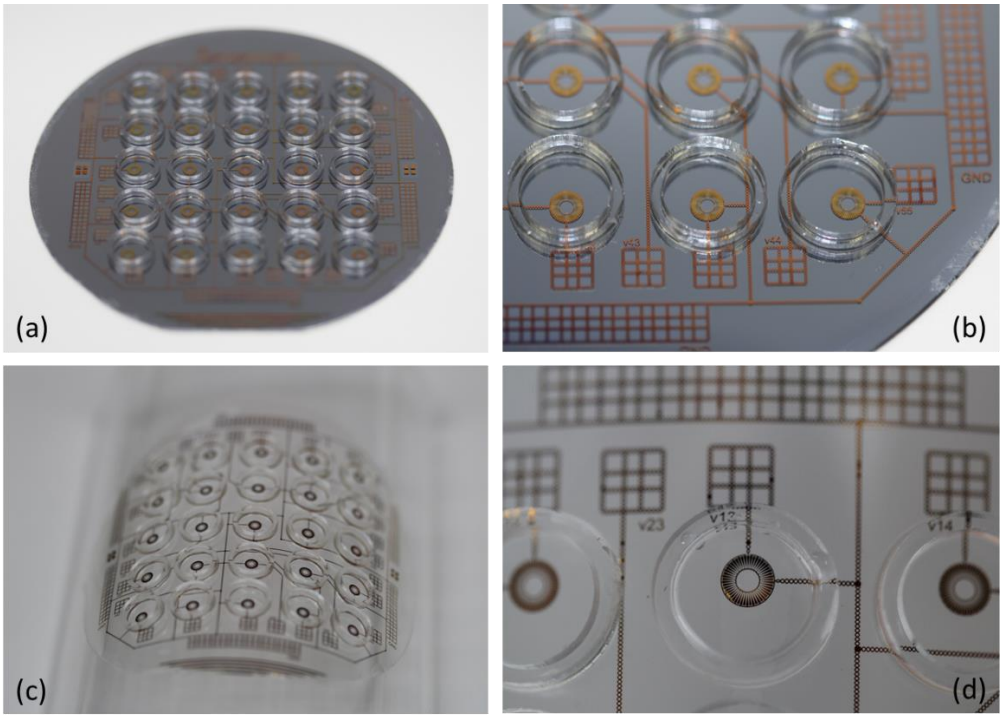

Figure 4.3. *Photographs of* ***(a)*** *a 5 × 5 electrowetting on dielectric (EWOD) tunable lens array while still on a silicon carrier wafer used to ease the fabrication process,* ***(b)*** *a closer view of the lenses and contact pads of the array,* ***(c)*** *the PDMS sheet wrapped around a cylinder of a radius r = 70 mm,* ***(d)*** *a close-up view of a single, filled liquid lens in the array.*

4.3. Results

Once fabrication and assembly had been completed, individual lenses of the array were individually characterized before being used as an array. The first step was to examine how much actuation occurred within the lenses as voltage was applied across interdigitated electrodes. This actuation was first observed with the use of a microscope to measure how much the oil droplet was squeezed. These results can be seen in Figure 4.4. As expected, the oil droplet is initially pinned to the hydrophilic/hydrophobic boundary at the outer edge of the electrodes (see Figure 4.4a), but as increasing voltage is applied the water is attracted down and in towards the underlying electrodes, squeezing the oil droplet inwards. The measured current through the

device also increased with increased applied voltage. Current values measured only a few μA at low voltages and reached a maximum of 20.77 mA (RMS) at our maximum driving voltage (150 V peak-to-peak).

These values may initial lead to some fear concerning heating of the device due power consumption, since the power consumed by the lens can be described by equation 4.3

$$P_{avg} = I_{avg} V_{avg} \cos \varphi \tag{4.3}$$

where P is the average power, I is the average (RMS) current, V is the average (RMS) voltage and φ is the phase angle between the voltage and the current. However, the capacitance of the circuit which comprises each of our liquid lenses has a capacitance on the order of 10 pF, and all applied voltages were AC square waves at 10 kHz. This means the overall impedance of the circuit is approximately 1.6 MΩ with a phase angle very near -90°. We ran most of our lens at a peak driving voltage of 100V peak-to-peak square wave (50V RMS) and measured a corresponding current of approximately 13mA (RMS). This yields a average power of approximately 0.2 mW. The joule heating of a system is can be described by equation 4.4

$$Q = c\, m\, \Delta T \tag{4.4}$$

where Q is joules, or watt-seconds, c is the specific heat of an object, and ΔT is the change in temperature. If we consider the volume of liquid in our lens chamber as a heat sink, and observe that the overwhelming majority of the liquid it water, we can take the mass of water need to fill our well as m and the specific heat of water as c. This means that we would expect a temperature increase of only 0.005 °C/second while the lens is powered at 100V. Thus, we need not be concerned about affects of heating on our microlenses.

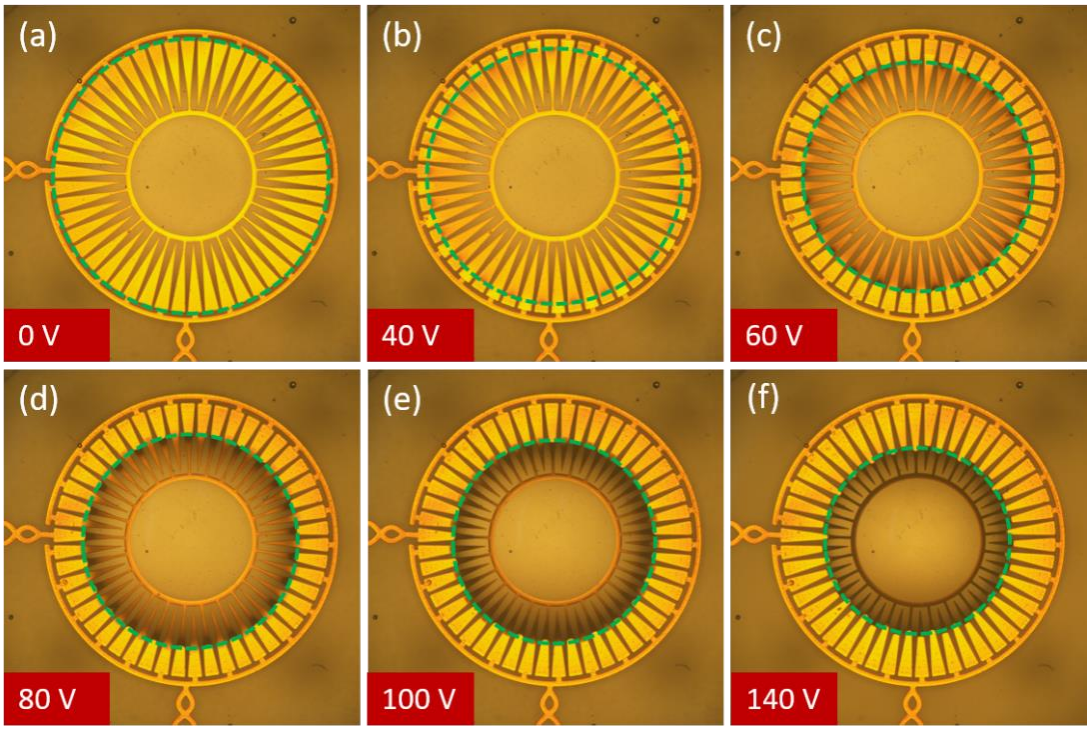

Figure 4.4. *Images of a single lens during actuation, where all applied voltages are AC square waves at 10 kHz, all values peak-to-peak. The dashed green circles have been added to highlight the boundary between the oil droplet and the water that surrounds it.* ***(a)*** *The initial, rest state of the lens. With no applied voltage the oil droplet is pinned at the hydrophilic/hydrophobic boundary.* ***(b)*** *At 40 V, the oil droplet has begun to be squeezed as the water is attracted toward the underlying electrodes. This squeezing increases steadily with increased applied voltage as seen in* ***(c)*** *at 60 V,* ***(d)*** *at 80 V,* ***(e)*** *at 100 V and finally* ***(f)*** *at 140 V.*

In order to get more information about the change in shape of the oil droplet as voltage is applied we also observed the profile view of the lens. This was done using a goniometer (OCA 15+, DataPhysics Instruments Inc., Filderstadt, Germany), which allowed us to measure the change in contact angle with respect to voltage, as well as extract the surface profile of the lens at any given voltage. From the contact angle we can observe radius of curvature of our lens with respect to voltage and use this information to directly compute the focal length of the lens. These

goniometer results can be seen in Figure 4.5, where we observed a change in the contact angle from 29.0° to 52.7° for a range of voltages from 0 V to 110 V. From the goniometer and microscope results, we can also find the range of focal length for our lenses. Since silicone oil has a higher index of refraction than water, the lens will always have a positive focal length, which shortens as increasing voltage is applied. We found such focal length range to be from 20.2 mm to 9.2 mm.

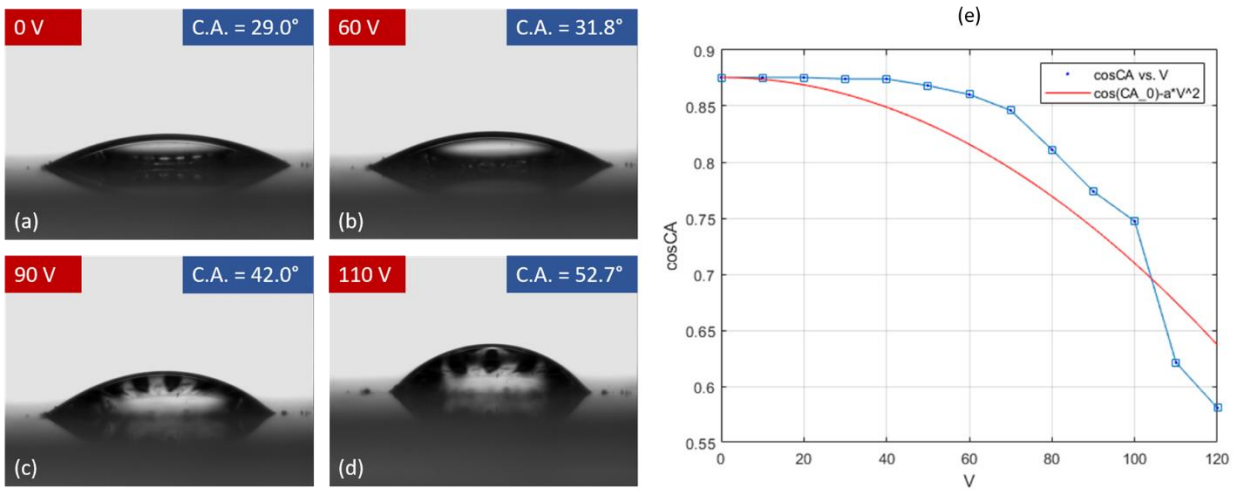

Figure 4.5. *Goniometer images (profile view) of the lens formed by a silicone oil droplet surrounded by water (10 kHz square wave, all values peak-to-peak).* ***(a)*** *Initial rest state of lens with contact angle of 29.0° at 0 V.* ***(b)*** *The contact angle of the oil droplet increases to 31.8° at 60 V applied, corresponding to a decrease in the radius of curvature of the lens.* ***(c)*** *Contact angle of 42.0° at 90 V.* ***(d)*** *Contact angle of 52.7° at 110 V.* ***(e)*** *Plot of the cosine of the contact angle vs vs. the driving voltage (oil volume: 0.6253 μL) in blue. The red line shows a curve fit of that data according to equation (4.1).*

While the goniometer allowed us to observe a 2D surface profile of the liquid lens shape during electrowetting, we were able to acquire more complete, 3D information about the lens shape by using a Shack–Hartman wavefront sensor (SHWS) [17,18]. A SHWS consists of a dense, uniform microlens array and a digital detector. When a plane wave impinges squarely on

the SHWS, each microlens focuses this planewave into a point in the center of its cell. When a wavefront of a different shape (for instance a spherical wavefront) impinges on the SHWS the angle of the wave in a small area can be determined by measuring the displacement of the focal spot from the center. This data can be reconstructed across the whole sensor to make a measurement of the shape of the wavefront. In Figure 4.6 we can again see that the effective focal length of the lens shortens with increasing applied voltage.

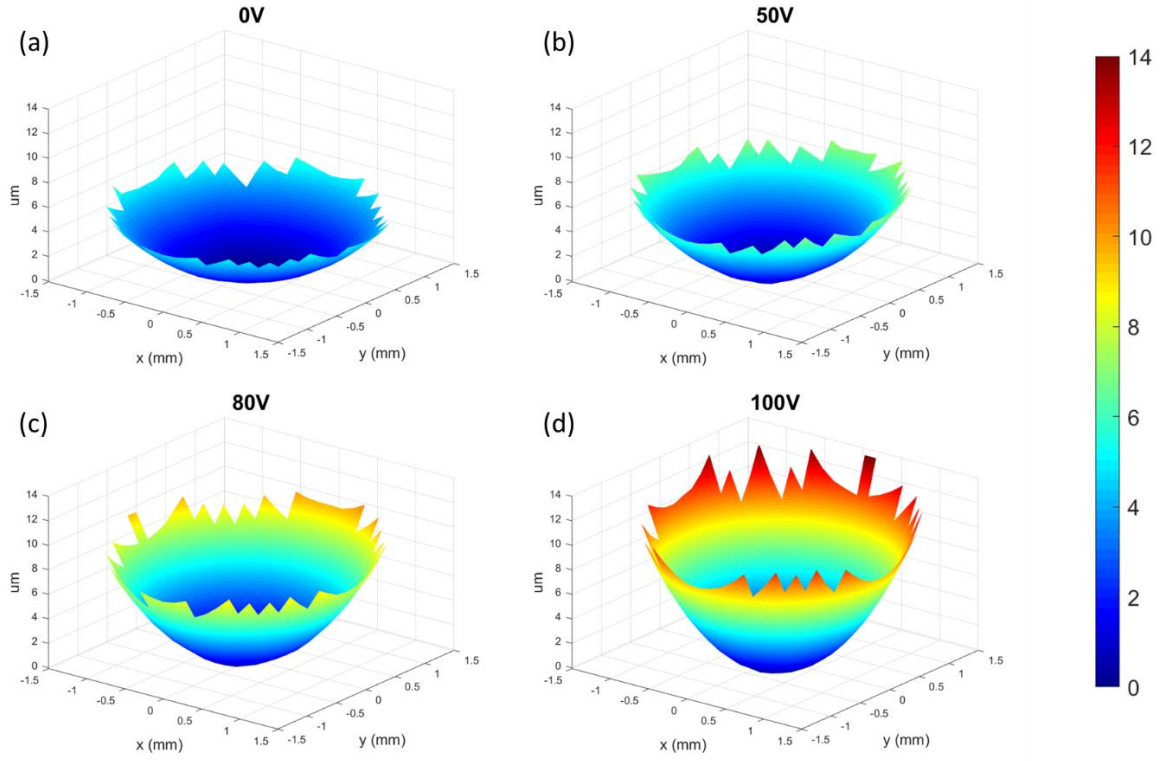

Figure 4.6. *Plots generated by a Shack–Hartmann wavefront sensor showing the shape of a plane wave (from a 5mA HeNe laser) after it has passed through the lens under different levels of actuation. The z-scale and corresponding color bar units are in μm (10 kHz square wave, all values peak-to-peak).* ***(a)*** *Initial wavefront shape with 0 V applied;* ***(b)*** *50 V applied;* ***(c)*** *80 V applied;* ***(d)*** *100 V applied.*

The wavefront data collected by the SHWS (WFS150C, Thorlabs Inc., Newton, NJ, USA) was also fit to the Zernike polynomials, which are a radial basis set often used to describe

wavefronts. This allows the wavefront to be decomposed into Zernike modes, which allows for description of wave aberration functions. We fit the data collected by the SHWS to the orthonormal Zernike functions up to the fourth order, which produces the coefficients of each Zernike mode, each of which corresponding to a different type of optical aberration [19]. This information can be seen in Table 4.1. It should be noted that the fit for determining Zernike modes was very good for all measurements, with mean fit errors on the order of 1×10^{-11} arcmin or lower and standard deviations fit errors on the order of 1×10^{-4} arcmin. The wavefront sensor data was then fed into ZEMAX, which was used to simulate the modulation transfer function (MTF) of the lens according to the method in [17]. The value of the MTF at 50% is reported in Table 4.2 along with the focal length of the lens. As expected, the MTF-50 value increases as the focal length decreases and the f-number (f/#) of the lens increases.

From our SWHS analysis, we expect to be able to form a good quality image with the liquid lenses of our array. To directly observe the imaging capabilities of our lenses we first set up a simple imaging system on our microscope. This was done by placing an optical object (1951 USAF resolution target) on the stage of the microscope, and then raising the lens 4.42 mm above the object using spacers. The resulting virtual image (formed because the object was within the focal length of the lens) was then brought into focus through the microscope objective. As voltage was applied to the system the oil droplet was squeezed inwards, increasing the radius of curvature and shortening the focal length of the lens. After each change in applied voltage the focal plane of the microscope was adjusted to bring the image formed by the lens back into focus. These images can be seen in Figure 4.7. This shortening of the focal length corresponds to an increasing image distance. Since the object distance does not change, this results in the magnification of the resulting image as applied voltage increases.

Table 4.1. *Zernike coefficients (in μm) of our lens at different applied voltages, corresponding to the wavefronts shown in Figure 4.6. Note that n refers to the radial order of the polynomial and m refers to angular frequency.*

Index[1]	(n,m)	Mode name	Zernike Coefficients			
			0 V	**50 V**	**80 V**	**100 V**
0	(0,0)	Piston	−1.418	−2.605	−2.903	−3.966
1	(1,-1)	Tilt y	0.024	0.164	−0.214	−0.729
2	(1, 1)	Tilt x	−0.061	0.171	0.247	1.001
3	(2,-2)	Astigmatism ±45°	−0.05	0.076	0.026	−0.032
4	(2,0)	Defocus/Power	1.525	2.093	2.777	3.675
5	(2,2)	Astigmatism 0/90°	0.006	0.060	0.011	−0.012
7	(3,-1)	Coma x	−0.004	0.000	0.016	0.033
8	(3,1)	Coma y	−0.029	−0.001	−0.029	−0.031
12	(4,0)	Spherical	0.034	0.013	0.063	0.100

[1] OSA/ANSI index numbering for Zernike modes

Table 4.2. *Measured focal length of the lens and MTF-50 values simulated in ZEMAX from Shack–Hartmann wavefront sensor data reported in Figure 4.6 and Table 4.1.*

	0 V	**50 V**	**80 V**	**100 V**
Focal length (mm)	20.30	17.27	12.39	9.62
Simulated MTF-50 (cycles/mm)	15	34	35	56

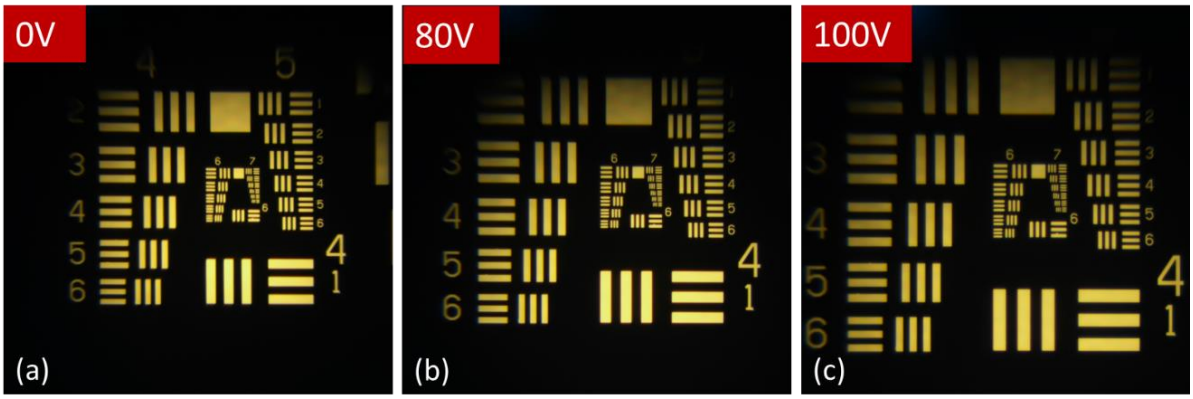

Figure 4.7. *Images produced by a lens at different levels of actuation. As increasing voltage is applied the radius of curvature of the liquid lens decreases. Since the object distance remains fixed, the image produced is magnified with decreasing focal length, as expected.* ***(a)*** *Microscope image produced by focusing the microscope to the image plane produced by the convex lens at its initial rest state of 0 V applied.* ***(b)*** *80 V is applied to the lens and the microscope focus is readjusted to match the new image plane of the lens, resulting in a larger image of the object.* ***(c)*** *When 100 V is applied to drive the lens, the microscope focus is again readjusted to produce a still-larger image.*

The same set up used in Figure 4.7 was also utilized to conduct direct focal length measurements of the lens with respect to applied voltage, the results of which can be seen in Figure 4.8. The lens exhibited a large range of achievable focal lengths, and we observed that the focal length tuning of the lens also exhibited hysteresis, a very common characteristic of electrowetting lenses which results from the difference between the advancing and receding edge of a liquid droplet in motion.

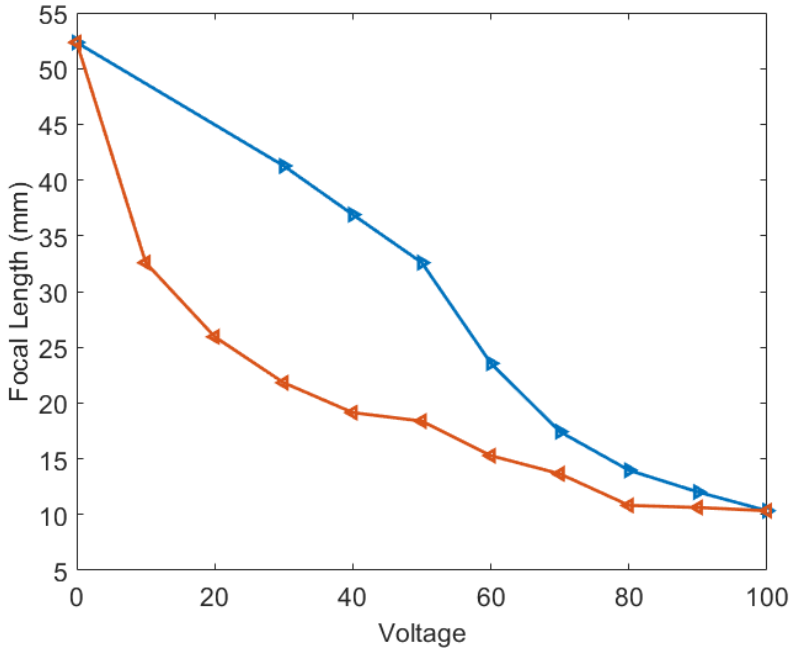

Figure 4.8. *A plot of the focal length vs applied voltage of the lens used to image the 1951 USAF resolution target in Figure 4.7. The lens exhibits clear hysteresis, as expected in electrowetting lenses. The line in blue with triangles to the right shows the lens with increasing voltage, while the line in orange with triangles to the left shows the focal length as applied voltage is decreased.*

The final step in the process was to test the functionality of the array of lenses on our flexible sheet. In order to demonstrate improvement in the potential FOV of our system we obtained images from the central 3 × 3 lenses of the sheet when it was both flat and when it was wrapped on a convex curve, respectively. The setup used to obtain such images was constructed on an optical table and was composed of four basic components: a large optical object, in this case a printed scene including several crests; the flexible sheet containing the liquid lenses; an opaque, rigid sheet with an array of 1mm apertures over which the lenses of the flexible sheet were centered; and a small CMOS image sensor mounted on a 3-axis stage for precise positioning required to obtain images from each lens in the array. We used stereolithography (3D

printing) to produce two different structures that contained the array of apertures. The first was flat and the second was curved, conforming to part of a cylinder with a radius of curvature of 70 mm. The optical object was placed 87 cm away from the flexible sheet of lenses. Images were first obtained by the nine lenses in the flexible sheet while it was laid over the flat aperture array. These images were then stitched together into a single image using the computer vision toolbox in MATLAB. The resulting image is shown in Figure 4.9a and has a FOV of 21.5°. Next, the flexible sheet of lenses was wrapped around the curved aperture array and images were again obtained from all 9 lenses. The same process was used to stitch these images together, the result of which can be seen in Figure 4.9b. The FOV increased significantly, up to 40.4°.

Using this same setup, we also obtained the resolution of our system. This was done using a standard 1951-U.S. Air Force target as the optical object, as shown in Figure 4.9c, yielding an angular resolution of 0.7 milliradians. This is only slightly below the theoretical resolution limit for the system of 0.61 mrad, approximated by the Rayleigh criterion for a circular aperture of a diameter equal to 1 mm and a wavelength of 500 nm. There are a number of possible sources of aberrations that lead to this decrease in resolution, among which is the tendency of liquid lenses to exhibit spherical aberration, as discussed earlier, and the possibility of contamination of the electrowetting surface by dust particles, which can lead to small asymmetries in lens actuation. This dust contamination can occur during the final filling of the lenses with the two immiscible liquids, which takes place outside of the cleanroom environment. Other potential sources of aberrations include the effect of the interdigitated electrodes, which squeeze the oil directly over the copper electrodes more strongly than the oil over the gaps in between. This leads to a slight scalloping effect at the edges while the lens is being actuated, which may introduce small aberrations.

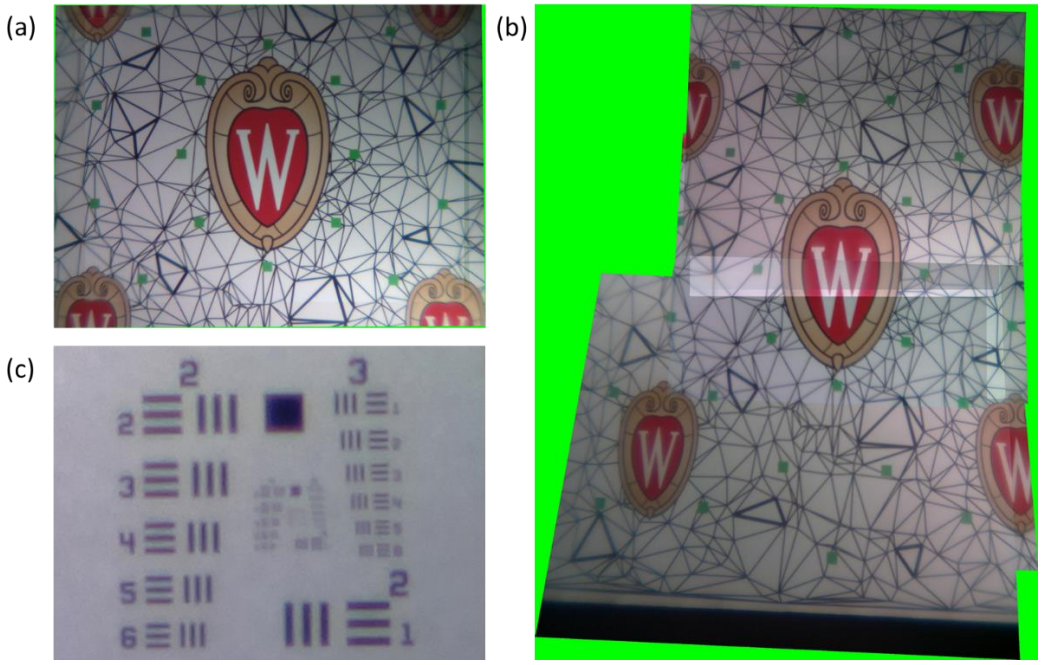

Figure 4.9. (a) *A stitched image composed of nine separate images from the central 3 × 3 section of the array while the flexible sheet is on a flat surface. When on a flat surface the system has an FOV of 21.5°.* ***(b)*** *A stitched image composed from images obtained from the same central 3 × 3 section of the array, only now wrapped around a curved surface (radius equal to 70 mm). The FOV is increased significantly in the direction of curvature, up to 40.4°.* ***(c)*** *An image of a 1951-USAF resolution target obtained from one of the lenses in the array. Smallest resolvable line pair is group 3, element 6, corresponding to 14.25-line pairs/mm, or an angular resolution of 0.7 mrad. Similar results were obtained for other lenses in the array.*

4.4. Discussion

We have detailed a successful fabrication method for constructing a 5 × 5 array of independently tunable, EWOD microlenses on a flexible sheet. This method improved on previous designs by changing materials to allow for a more stable hydrophobic/hydrophilic boundary necessary to define the rest state of the lens, and by reducing the thickness of the dielectric layer, which allowed for increased amount of actuation at applied voltages. The quality

of our dielectric layer ensured that all lenses were robust against dielectric breakdown at voltages of 120 V or less, and many were robust at even greater voltages. When breakdown did occur, it was usually due to shorts through pinhole defects in the dielectric, occurring at high voltages and leading to bubbling in the lens. This actuation was observed and characterized using a variety of methods, including a top-down view of the change in oil droplet shape on the microscope, and a profile view of the change in contact angle as a function of applied voltage captured on a goniometer.

Characterization of the optical properties of our microlenses incorporated measurements with a SHWS to collect wavefront data in order to assess the shape of the lens. This data was then fit with Zernike polynomials. Spherical aberration is the most consistent and pronounced source of aberrations for our lenses and is a common characteristic of liquid lenses. However, the fact that only the central section of our liquid lens is utilized for imaging (the region where there are electrodes in the optical path) helped to minimize this aberration. We also conducted a preliminary verification of focal length tuning by observing the magnification of an image formed by the lens at close range to the object and again captured on the microscope.

Finally, we demonstrated the functionality of a 3 × 3 section of our array on both a planar surface and on a cylindrical one. This testing was performed with a large object at distance (on the order of 1 m). Images were acquired from each of the nine lenses in the array for each configuration and then stitched into a single, larger image allowing us to demonstrate improvements in the FOV, nearly doubling on our cylindrical surface as compared to planar. Additionally, since there was more than sufficient overlap between all images in the array for stitching, even in the cylindrical arrangement, future work might see even larger improvements in FOV for the flexible sheet.

References

[1] Lu, Y.S.; Tu, H.; Xu, Y.; Jiang, H. Tunable dielectric liquid lens on flexible substrate. *Appl. Phys. Lett*. **2013**, *103*, 261113.

[2] Li, C.; Jiang, H. Fabrication and characterization of flexible electrowetting on dielectrics (EWOD) microlens. *Micromachines* **2014**, *5*, 432–441.

[3] Van Grinsven, K.L.; Ousati Ashtiani, A.; Jiang, H. Fabrication of an Electrowetting Microlens Array on a Flexible Substrate. In Proceedings of the 19th International Conference on Solid-State Sensors, Actuators and Microsystems (TRANSDUCERS), Kaohsiung, Taiwan, China, 18–22 June 2017; pp. 1983–1986.

[4] Shahini, A.; Xia, J.; Zhou, Z.; Zhao, Y.; Cheng, M.M.C. Versatile Miniature Tunable Liquid Lenses Using Transparent Graphene Electrodes. *Langmuir* **2016**, *32*, 1658–1665.

[5] Wei, K.; Zhao, Y. A three-dimensional deformable liquid lens array for directional and wide angle laparoscopic imaging. In Proceedings of the IEEE International Conference on Micro Electro Mechanical Systems (MEMS), Taipei, Taiwan, China, 20–24 January 2013; pp. 133–136.

[6] Chandra, D.; Yang, S.; Lin, P.C. Strain responsive concave and convex microlens arrays. *Appl. Phys. Lett*. **2007**, *91*, 251912.

[7] Chronis, N.; Liu, G.L.; Jeong, K.H.; Lee, L.P. Tunable liquid-filled microlens array integrated with microfluidic network. *Opt. Express* **2003**, *11*, 2370–2378.

[8] Ren, H.; Wu, S.T. Tunable-focus liquid microlens array using dielectrophoretic effect. *Opt. Express* **2008**, *16*, 2646–2652.

[9] Miccio, L.; Finizio, A.; Grilli, S.; Vespini, V.; Paturzo, M.; De Nicola, S.; Ferraro, P. Tunable liquid microlens arrays in electrode-less configuration and their accurate characterization by interference microscopy. *Opt. Express* **2009**, *17*, 2487–2499.

[10] Ren, H.; Fan, Y.H.; Gauza, S.; Wu, S.T. Tunable microlens arrays using polymer network liquid crystal. *Opt. Commun*. **2004**, *230*, 267–271.

[11] Ousati Ashtiani, A.; Jiang, H. Design and fabrication of an electrohydrodynamically actuated microlens with areal density modulated electrodes. *J. Micromech. Microeng*. **2016**, *26*, 015004.

[12] Van Grinsven, K.L.; Ousati Ashtiani, A.; Jiang, H. Fabrication and Actuation of an Electrowetting Droplet Array on a Flexible Substrate. *Micromachines* **2017**, *8*, 334.

[13] Liu, C.; Park, J.; Choi, J. A planar lens based on the electrowetting of two immiscible liquids. *J. Micromech. Microeng*. **2008**, *18*, 035023.

[14] Wang, W.; Kang, D.; Tai, Y.C. Study of Parylene penetration into microchannel. In Proceedings of the 18th International Conference on Solid-State Sensors, Actuators and Microsystems, TRANSDUCERS 2015, Anchorage, AK, USA, 21–25 June 2015; pp. 1307–1310.

[15] Kahouli, A.; Sylvestre, A.; Jomni, F.; André, E.; Garden, J.L.; Yangui, B.; Berge, B.; Legrand, J. Dielectric properties of parylene AF4 as low-k material for microelectronic applications. *Thin Solid Film*. **2012**, *520*, 2493–2497.

[16] Dolbier, W.R.; Beach, W.F. Parylene-AF4: A polymer with exceptional dielectric and thermal properties. *J. Fluor. Chem*. **2003**, *122*, 97–104.

[17] Li, C.; Hall, G.; Zhu, D.; Li, H.; Eliceiri, K.W.; Jiang, H. Three-dimensional surface profile measurement of microlenses using the Shack–hartmann wavefront sensor. *J. Microelectromech. Syst.* **2012**, *21*, 530–540.

[18] Li, C.; Hall, G.; Zeng, X.; Zhu, D.; Eliceiri, K.; Jiang, H. Three-dimensional surface profiling and optical characterization of liquid microlens using a Shack–Hartmann wave front sensor. *Appl. Phys. Lett*. **2011**, *98*, 171104.

[19] Rahbar, K.; Faez, K.; Attaran Kakhki, E. Phase wavefront aberration modeling using Zernike and pseudo-Zernike polynomials. *J. Opt. Soc. Am. A* **2013**, *30*, 1988–1993.

5. Magnetically Actuated Liquid Lens

5.1 Introduction

Using electromagnetism and taking advantage of the inherent relationship between electricity and magnetism in order to achieve linear actuation has been taking place for decades. It is the basis of such well established technology as the voice coil actuators, which utilize an electrical coil and a permanent magnet to translate the movable portion of the system in a piston motion [1–3]. Voice coil actuators are fast and precise, though they can be prone to long-term wear. Electromagnetism has been used as the actuating force for a number of different kinds of tunable lenses and optical systems as well, though there is a large variety of configurations of electromagnet/wiring and permanent magnet [4–6]. Many, like ours, utilize a membrane to transfer actuation from one region of a chamber to another in order to ensure a clear optical path for the lens. In the following sections we will seek to take advantage of the force generated by the cross product of moving charge in a magnetic field in order to design and test a lens of our own configuration.

5.2 Actuation Mechanism

We have designed a liquid lens comprised to two chambers of density matched liquids of different indices of refraction separated by a PDMS membrane and shown in Figure 5.1. The lens itself is located in the central circular region of the two chambers. The area surrounding this central region holds a permanent magnet with radial magnetic field on one side of the PDMS membrane and a flat, circular winding of wire on the other side of the membrane. To define the diameter of our lens the membrane is pinned in place by a ring of posts which hold the membrane in place at the edges of the lens, but allow liquid to pass back and forth between the

central region where the lens is located and the outer regions, where the the winding and permanent magnet are housed.

When current is run through the winding, the movement of charge through the magnetic field of the permanent magnet generates a force, known as the Lorentz force. The Lorentz force for a point charge is given by Equation (5.1)

$$\vec{F} = q\vec{v} \times \vec{B} \tag{5.1}$$

where q is the value of the charge, v is the velocity of the charge, and B is the magnetic field through which it moves. In the case of our system we can generalize this Lorentz force the following equation (Equation (5.2))

$$\vec{F} = I\,\overrightarrow{dl} \times \vec{B} \tag{5.2}$$

where I is the current, dl is the a differential length of the winding cross section (which defines the direction the current is constrained to flow in), and B is again the magnetic field.

We can induce a steady current through the winding by applying a DC voltage differential across the length of wire which composes the winding. As demonstrated in Figure 5.1 we see that when a current is run clockwise (when viewed from the top) through the winding the Lorentz force will mean that the winding is attracted down towards the magnet, which is fixed in its housing. Since the PDMS membrane is between the winding and the magnet (and the winding is affixed to the membrane) the movement of the winding in response to the exerted Lorentz force displaces water which had previously filled the region between the winding and the magnet. Since liquids are incompressible, this displaced volume of water is simply transferred to the central region of the chamber, where the membrane bulges upwards by a volume equal to the volume displaces the attractive force to form the lens, as see in Figure 5.1b.

Since the index of refraction of silicone oil is greater that that of water (1.49 and 1.33 respectively) a diverging lens is formed.

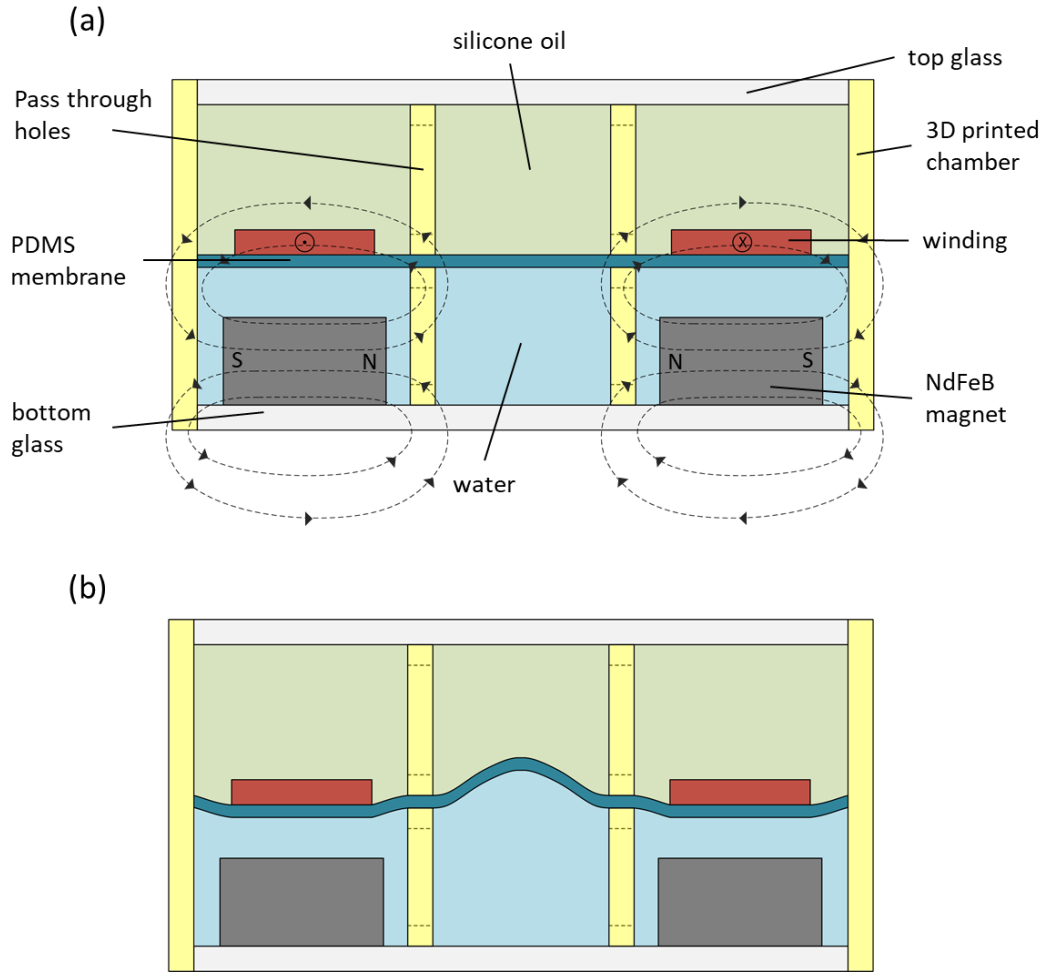

Figure 5.1. ***(a)*** *Cross section of the magnetically actuated liquid tunable lens. Radial magnetic fields are shown as dashed lines and arrows in the magnet show the direction of the field. Cross and dot in the winding show current direction (into page and out of page, respectively).* ***(b)*** *the lens in the actuated state, which shows a deformed membrane in the middle, which forms the liquid lens in the presence of electrical current.*

If the direction of the current were reversed (i.e., if it were applied to run in a counter-clockwise direction) then the cross product means that the direction of the Lorentz force is reversed, and the winding is repelled by the permanent magnet instead of attracted to it. This

displaces the silicone oil in the region of the chamber above the winding into the central section of the chamber, causing the membrane to bulge downwards there. This results in a converging lens. Thus, the power of the lens is proportional to the amount of current run through the winding, where higher current leads to a higher power lens, and the sign of the lens (whether it is diverging or converging) is determined by the direction of the current.

Other factors that will affect the power of the lens at a given current are the strength of the magnetic field, which depends on the material/strength of the permanent magnet and the distance of the winding from that magnet. The thickness of the PDMS membrane will also affect the power of the lens, since a thicker membrane will be stiffer, and thus require a high force to move. Finally, the amount of current we can run through our winding will be limited by ohmic heating affects. In or design, we have tried to carefully balance these different factors.

5.4 Fabrication

In order to fabricate the lens, we chose to make the lens housing via 3D printing. Specifically, we used a stereolithography (SLA) 3D printer which has the ability to print photopolymer resin with an XY resolution of 150 μm and a layer thickness of 100 μm (Form 2, Formlabs Inc., Somerville, MA). The lens housing consists of two separate 3D prints, the upper chamber and the lower chamber (see Figure 5.2). The primary difference between the upper and lower chamber is that the lower chamber has a recessed holder where the permanent magnet can be attached and is thicker (to accommodate the thickness of our magnet). Since ‘clear’ photopolymer resins used in SLA are not optically transparent, we leave to top and bottom face of the 3D printed chamber open so that two inch sapphire wafers can be glued in place instead to form the upper and lower face of our liquid chambers.

The winding used in our design was made by taking 30 AWG copper wire with nylon insulation and winding it into a ring with a power drill and a custom jig. The jig helped ensure that the winding ring was tightly packed, at which point a silicone-based adhesive diluted with hexane was poured in. The hexane evaporated and the silicone cured, resulting in a ring of copper winding with an inner diameter of 25 mm, and outer diameter of 35 mm and a thickness of 2 mm. The winding used 10 meters of wire and had approximately 125 turns. After the adhesive had set the winding was removed from the jig.

At this stage we are ready to begin assembly the lens. This is done in two stages, first by assembly the top portion consisting of the upper chamber, actuator winding, and PDMS membrane, and then by assembly the bottom portion consisting of permanent magnet and lower housing. Once they are both done, they can be combined and filled with our two liquids to form the final lens. Fabrication of the top portion of the device required that we first create a thin PDMS membrane (approximately 40 μm thick) on a 3 inch dummy wafer made of glass. This was done by first spin coating a sacrificial layer of photoresist (AZ P4620, MicroChem Corp., Westborough, MA, USA) onto the wafer and soft baking it. After the soft bake was complete, PDMS was spin coated on the wafer at 3000 rpm for 30 seconds. The wafer was then transferred to a hot plate set at 100°C while the PDMS cured. Once the PDMS membrane had fully cured the actuator winding was glued to the center portion of the membrane using a silicone adhesive (Sil-Poxy, Smooth-On, Macungie, PA). The PDMS and winding on the dummy wafer were then fit into the housing's upper chamber and the outer rim which defines the upper liquid chamber was also affixed to the PDMS membrane using Sil-Poxy. This step can be seen in Figure 5.3a.

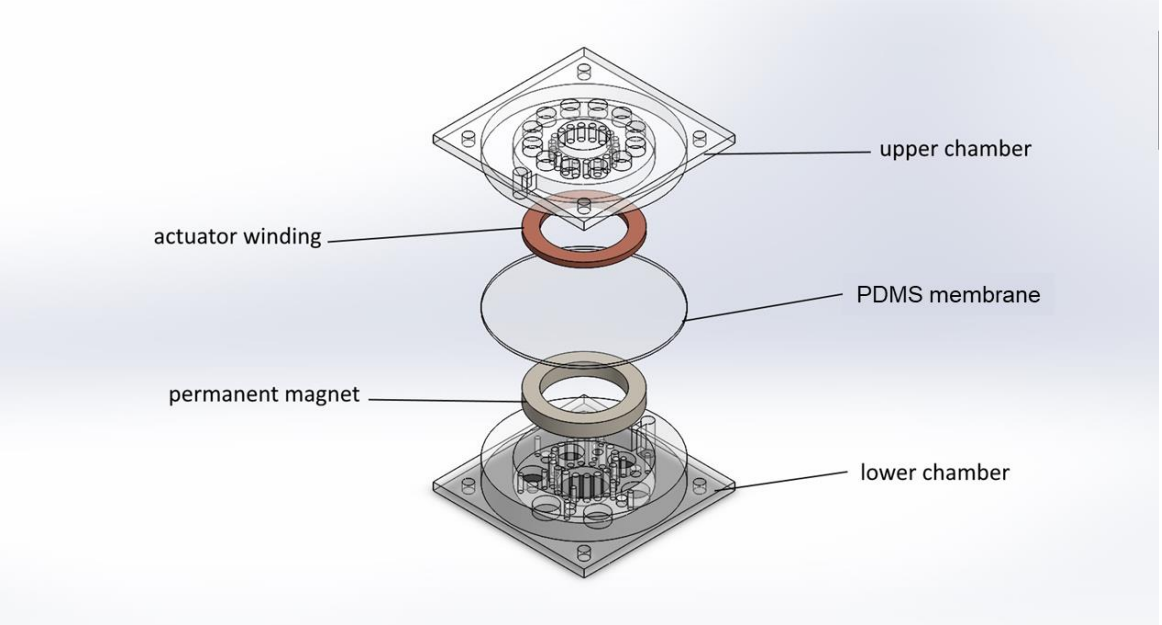

Figure 5.2. *Exploded view of the magnetically actuated liquid tunable lens, showing 3D printed upper and lower chamber, permanent ring magnet, copper wire winding, and PDMS membrane to define separate chambers for water and silicone oil.*

While the silicone adhesive was allowed to cure the permanent magnet was also fit into the lower housing and glued into place so that it remains stationary when the lens in in operation (see Figure 5.3b). The magnet used was a neodymium magnet (NdFeB) with inner diameter of 25 mm and outer diameter of 35 mm, which was magnetized such that north was on its inner radius and south is on the outer radius. The final step in preparing the two halves of the lens was to remove the PDMS membrane from the dummy wafer. This was done by submerging the upper half of the lens in a beaker of acetone and gently agitating it until the wafer lifted clear of the membrane. At this stage the two halves were glued together using epoxy, and once that epoxy had set epoxy was again used to attach the 2 inch sapphire wafer to the outside of both halves of our chamber to act as the faces of our liquid lens.

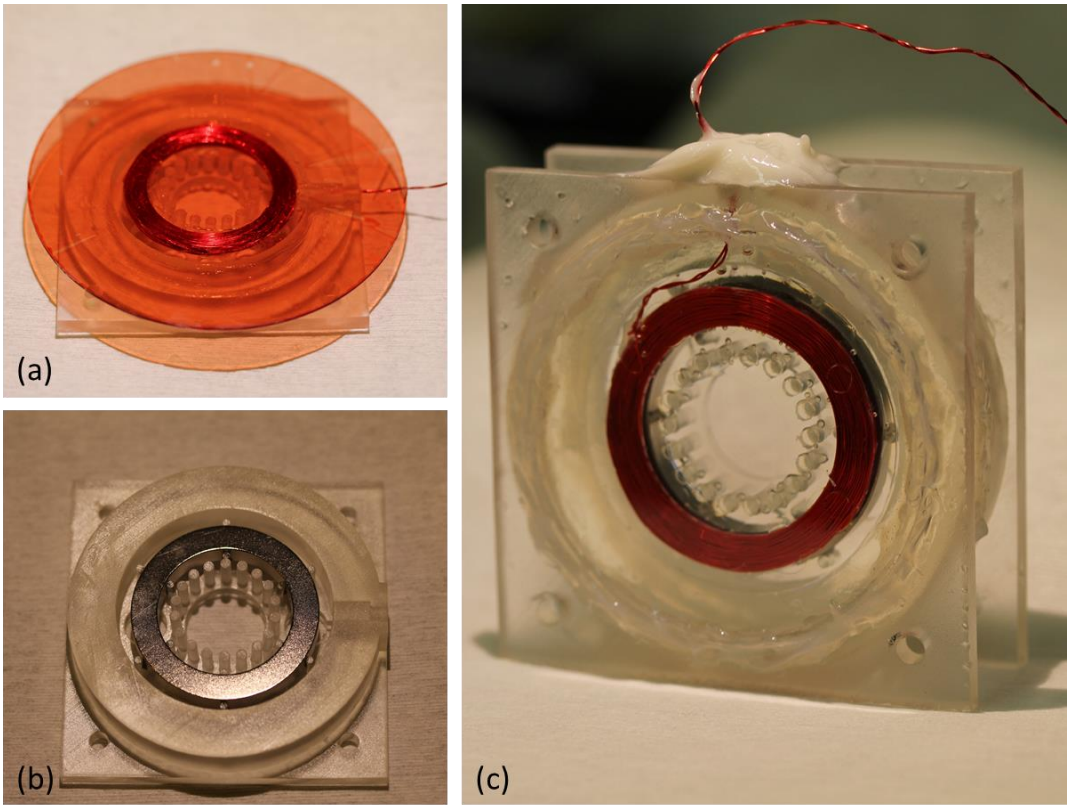

Figure 5.3. *Photographs of magnetically actuated lens at different stages of fabrication.* ***(a)*** *Upper half of 3D printed housing showing PDMS membrane on a glass dummy wafer, which has been glued to the winding and the housing.* ***(b)*** *Lower half of 3D printed housing, showing magnet mounted in place.* ***(c)*** *Fully assembled lens showing two halves of the housing glued together and 2" sapphire wafer sealed against both optical faces of the lens. The diameter of the liquid lens is defined by the ring of posts inside the winding.*

Our lens is now ready to be filled. This is done by slowly injecting water and oil into the two chambers through the ports built into our 3D printed housing. We fill the bottom chamber of the lens with water and the top chamber with silicone oil, and then seal the chamber entirely using a marine-grade epoxy, designed to cure in the presence of liquid. The completed liquid lens is pictured in Figure 5.3c.

5.5 Results

In order to characterize our magnetically actuated liquid lens, we first measured focal length vs. voltage. We choose to report applied voltages instead of applied current because we used a DC voltage source for our experiments (Agilent E3644A), but the current follows the voltage very linearly by the well known relation $I=V/R$, where the resistance of our system (the resistance of the copper winding) can be considered a constant for our purposes. In order to make measurements the focal length of the lens we needed a single set up that can measure the focal length of a both a diverging lens (formed when we apply a negative DC bias which results in a clockwise current) and of a converging lens (formed when we apply a positive DC bias, resulting in a counter-clockwise current).

A diagram of the optical setup we chose to implement for this purpose is showing in Figure 5.4a. It consisted of four components on a single, long optical rail: a CCD sensor, an auxiliary lens—in this case a plano-convex lens with focal length equal to 20 mm, the tunable lens itself, and a collimated beam from a HeNe laser. All components were aligned on the optical axis defined by the laser beam, and then the auxiliary lens was placed at a distance of twice its focal length from the CCD. On the other side of the auxiliary lens a resolution target was temporarily inserted at twice the focal length, at which point fine adjustments were made to the system such that the image of the target was brought into best focus on the CCD. The location of the target was marked on the optical rail as the image plane, and then the target was removed from the system and the tunable lens inserted.

Voltage was applied to the winding of the tunable lens ranging from -0.95 V to 0.95 V at intervals of 0.1 V. For each voltage the position of the tunable lens was adjusted until the laser beam was focused to the smallest possible point on the CCD. The distance between the marked

image plane and the face of the tunable lens furthest from the CCD gave the focal length of the magnetically actuated lens and recorded. When the lens is operating in the converging regime it will need to be positioned to the left of the marked image plane, so that the collimated beam will pass through it and then focus to a point at the image plane of the auxiliary lens and then be relayed to the CCD. This yields a positive focal length measurement. When the lens is operating in the diverging regime it will nee to be positioned to the right of the marked image plane such that the virtual point image formed by the liquid lens is located at the marked image place. This yields a negative focal length.

Graphs of measured focal length vs. applied voltage can be seen in Figure 5.4b. The measurement of the focal length for each applied voltage was repeated over 3 cycles in order to get an idea of the error of the measurement. The error bars of the graphs report the standard deviation of each measurement set. As we would expect, the error is greater at smaller applied voltages because such small amounts of actuation lead to very large radius of curvature of the lens, as shown by the Lensmaker's equation (5.3)

$$\frac{1}{f} = \frac{n_1 - n_2}{R} \tag{5.3}$$

where f is the focal length, R is the radius of curvature and n is the indices of refraction. At very large radii, the focal length of the lens becomes highly sensitive to even small changes of applied force.

We can also see in Figure 5.4b that the focal length range is greater when the lens is operating in the divergent regime as compared to when operating in the convergent regime. This occurs because in the divergent case the Lorentz force attract the winding closer to the magnet where the magnetic field is strong, while in the convergent case the Lorentz force repels the winding from the magnet, taking it to a region of weaker magnetic field.

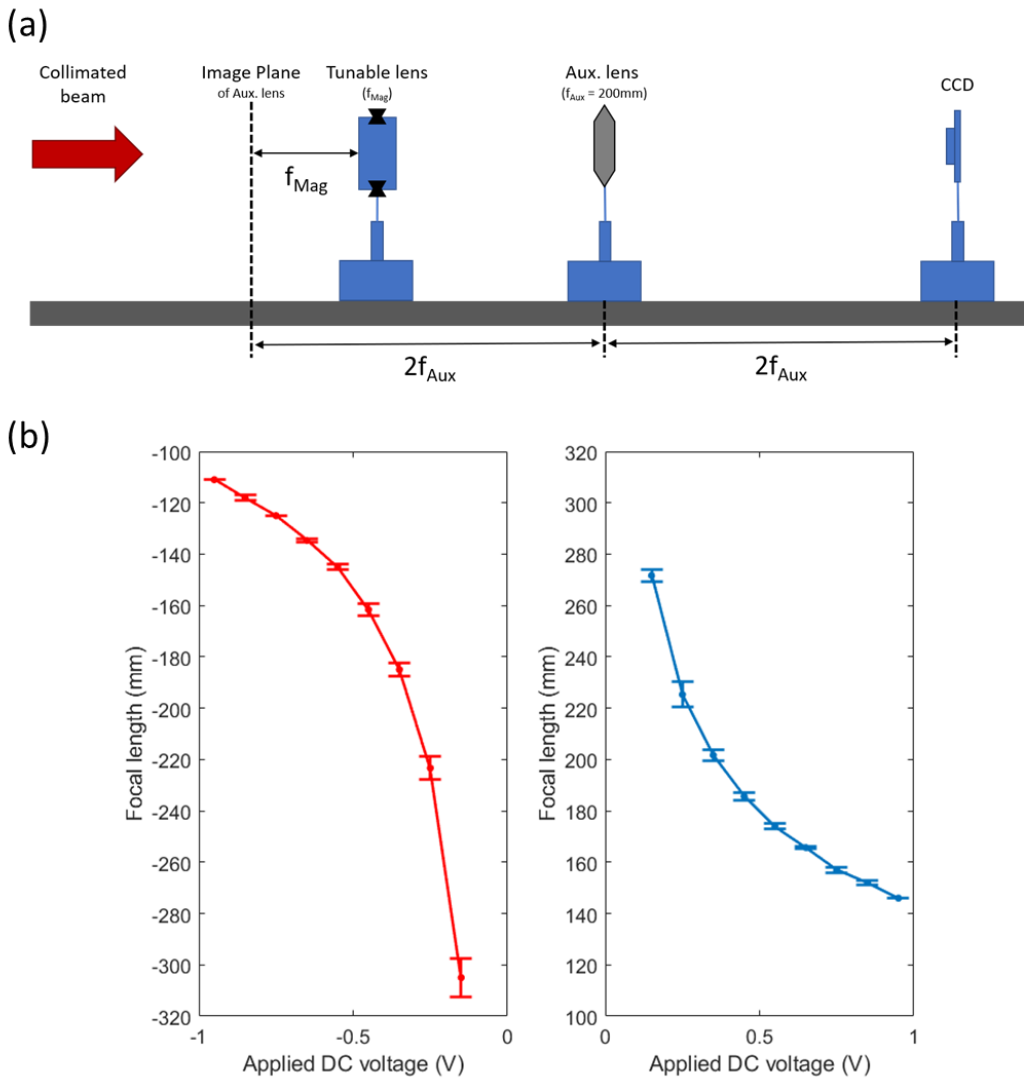

Figure 5.4. ***(a)*** *Diagram of experimental set up for measuring the focal length of the tunable lens. A collimated laser beam acts as an object at infinity and an auxiliary lens with 200 mm focal length was placed at a distance of 2f from a CCD detector and both were fixed in place. Then the tunable lens is allowed to slide along an optical rail and is adjusted until the light focuses to a point. The distance between the lens and the virtual object is the focal length.* ***(b)*** *Graph of lens focal length vs. applied voltage, with error bars showing standard deviation of the measurement under cycling. When negative voltages are applied the winding is repelled by the magnet and a concave lens (corresponding to a negative focal length) if formed. When positive voltages are applied the direction of current flow in reverse, meaning the winding is attracted to the magnet and a convex (positive focal length) lens is formed.*

The next measurement we conducted was to measure the shape of the wavefront produced by our tunable lens (Figure 5.5). This was done using a Shack-Hartmann wavefront sensor (SHWS). Our SHWS (WFS150C, Thorlabs Inc., Newton, NJ, USA) setup allowed us to measure the shape of the central 4.75 mm region our 15 mm diameter lens. At zero volts applied and no current through the wire we expect the wavefront to be essentially flat, but as we begin to apply voltage we observe an increasing curvature to the wavefront shape. The z-axis of the wavefront sensor points towards the sensor, so that when the impinging wavefront is diverging (concave lens) the shape of the plotted wavefront is mounded, with peak values in the center region. When we change the direction of the current the wavefront becomes converging (convex lens) and the shape of the plotted waveform is cupped, with peak values at the outer region. This data can also be fitted with Zernike polynomials in order to describe the aberrations of the lens, the results of which are shown in Table 5.1. The defocus/power term in the table is related to the radius of curvature of the wavefront, which is proportional to the radius of curvature of the lens itself, and we see the expected trend from large negative number to large positive number as we move from large negative applied voltages to large positive applied voltages. The Zernike data confirms that aberrations are generally small, though the most significant of them seems to be astigmatism. This may be a result of asymmetries caused by possible slight warping of the 3D printed housing where it pins the edge of the PDMS membrane, or inconsistency of the membrane itself.

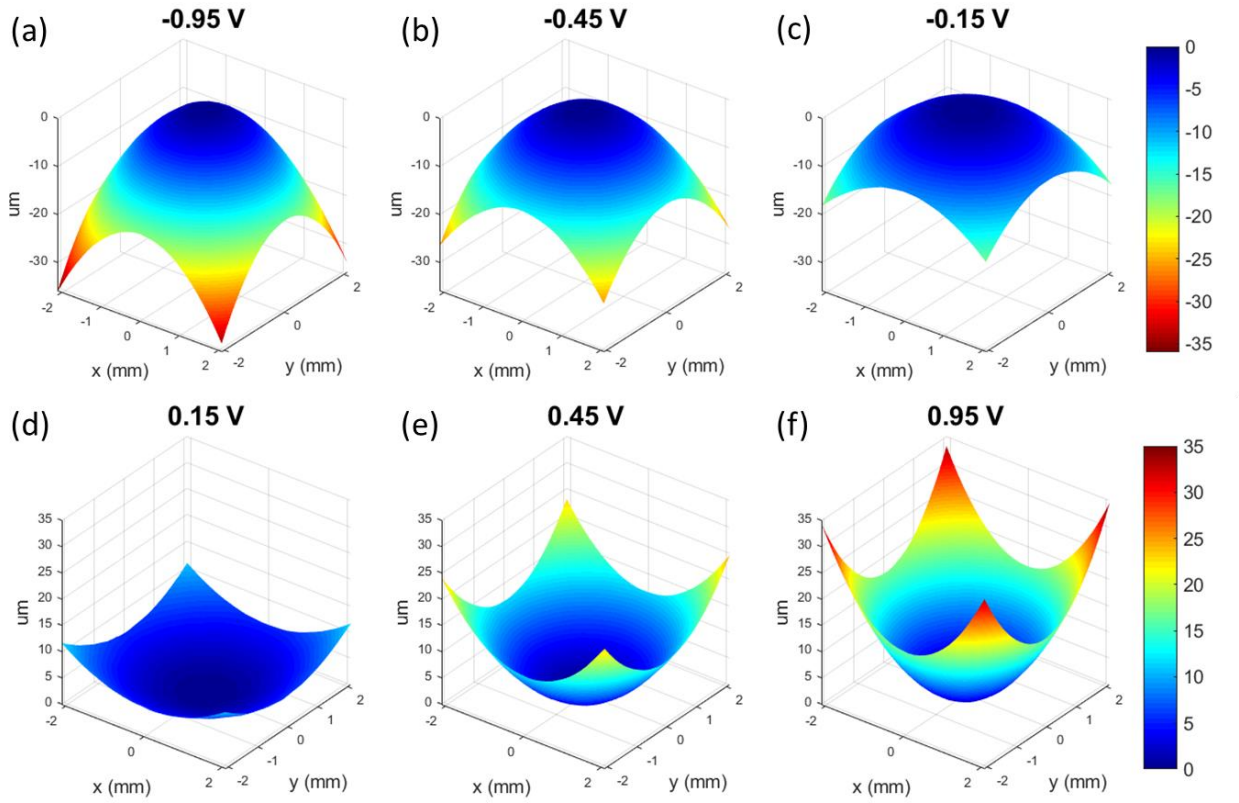

Figure 5.5. *Shack Hartmann wavefront sensor data from magnet lens at different levels of actuation.* ***(a)-(c)*** *Show the lens concave (diverging), where the increasingly large negative applied voltages lead to a concave lens with increasing optical power.* ***(d)-(f)*** *Show the lens convex (converging) where increasing applied voltages lead to increasing optical power of the lens.*

Table 5.1. *Zernike coefficients (in μm) of our lens at different applied voltages, corresponding to the wavefronts shown in Figure 5.5.*

Index	Mode name	Zernike Coefficients					
		-0.95 V	**-0.55 V**	**-0.15 V**	**0.15 V**	**0.55 V**	**0.95 V**
1	Piston	5.680	4.816	2.350	-2.047	-3.979	-5.291
2	Tilt y	0.676	0.511	0.444	-0.325	-0.945	-0.813
3	Tilt x	0.180	-0.004	0.454	-0.005	-0.349	-0.513
4	Astigmatism ±45°	-0.140	-0.123	-0.106	0.122	0.221	0.251
5	Defocus/Power	-6.380	-5.226	-3.259	2.062	4.804	6.137
6	Astigmatism 0/90°	-0.047	0.007	0.074	0.146	0.183	0.186
7	Trefoil y	-0.001	-0.009	0.008	0.023	0.003	-0.014
8	Coma x	-0.015	-0.012	-0.010	0.006	0.020	0.025
9	Coma y	0.007	0.010	0.012	-0.020	-0.019	-0.025
10	Trefoil x	-0.005	0.003	0.012	0.018	0.039	0.042

11	Tetrafoil y	0.017	0.013	0.006	0.011	0.003	0.000
12	2nd astigmatism y	0.009	0.005	0.005	0.001	-0.005	-0.003
13	Primary spherical	0.000	-0.001	-0.001	0.001	0.019	0.026
14	2nd astigmatism x	0.004	0.005	0.001	0.006	-0.007	-0.012
15	Tetrafoil x	0.014	0.004	0.010	0.004	0.011	0.004

The final step in characterizing the optical properties of our magnetically actuated lens is to use the lens for imaging and observe its performance. Due to the inherent differences of converging and diverging lenses, two different set ups were required to capture the performance of our tunable lens in these two separate regimes, though both utilized a Canon DSLR camera fitted with a macro lens (see Figure 5.6). To observe the image created by the lens in the converging regime we mounted the DSLR on an optical rail and manually set its focus to infinity. Our tunable lens was then placed a short distance in front of the DSLR, and an 1951 optical target was placed at the focal length of the tunable lens. For each change in applied voltage the target was moved to the new focal length of the tunable lens and a series of images were captured. This was done both with an image of a badger as well as with a 1951 USAF resolution target, the results of which are shown in Figure 5.7. We observe the magnification of the image with increasing voltage and also measured the resolution of the system at each voltage. The maximum resolution reached was 7.13 line pairs per mm and resolution increases as the f/# decreases, as we would expect.

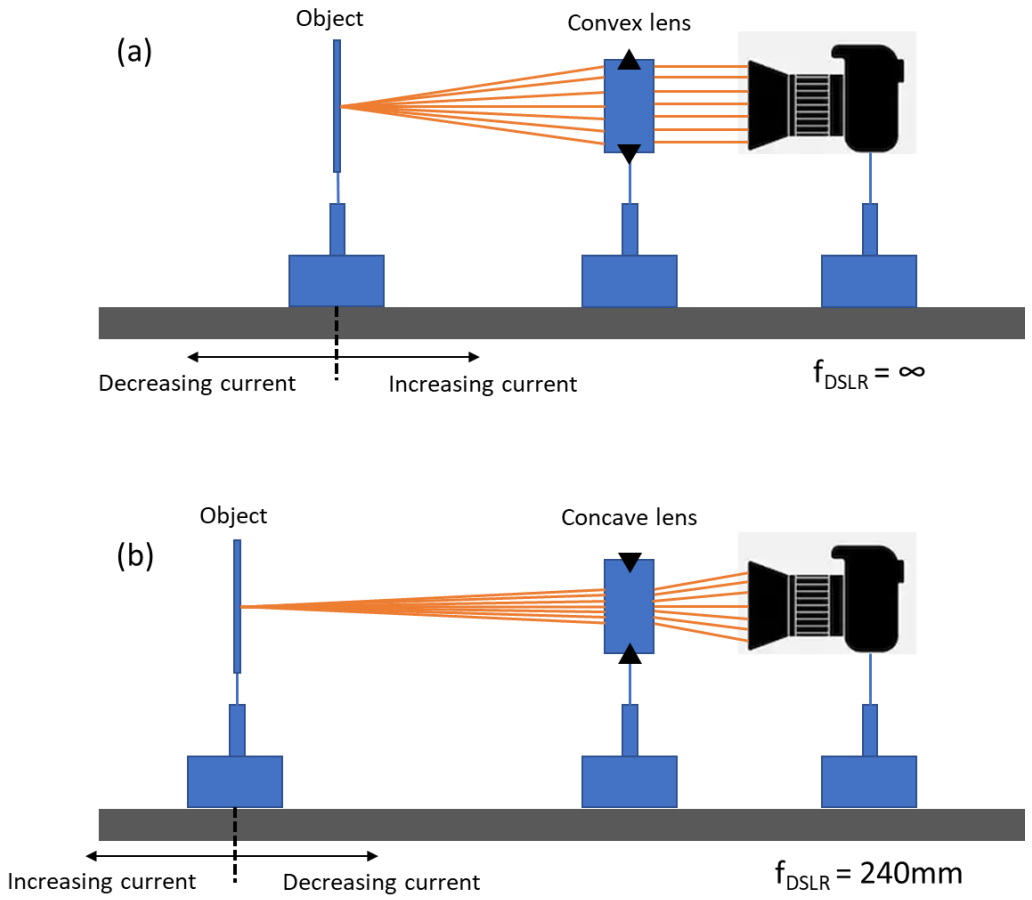

Figure 5.6. ***(a)*** *Diagram of optical setup used to image resolution chart and badger image when the tunable lens is operating in the converging regime (convex lens). A digital single-lens reflex (DSLR) camera with focal length set to infinity is placed on one side of the tunable lens, and an optical object is moved until it comes into the clearest focus.* ***(b)*** *Diagram of optical setup used when the tunable lens is operating in the diverging regime (concave lens). The focus of the DSLR is set to 240mm, and the optical object is moved until it comes it clearest focus. Since a stronger (more diverging) lens will shift the overall focus of the system to be longer, the object must be moved further away as current through the tunable lens increases.*

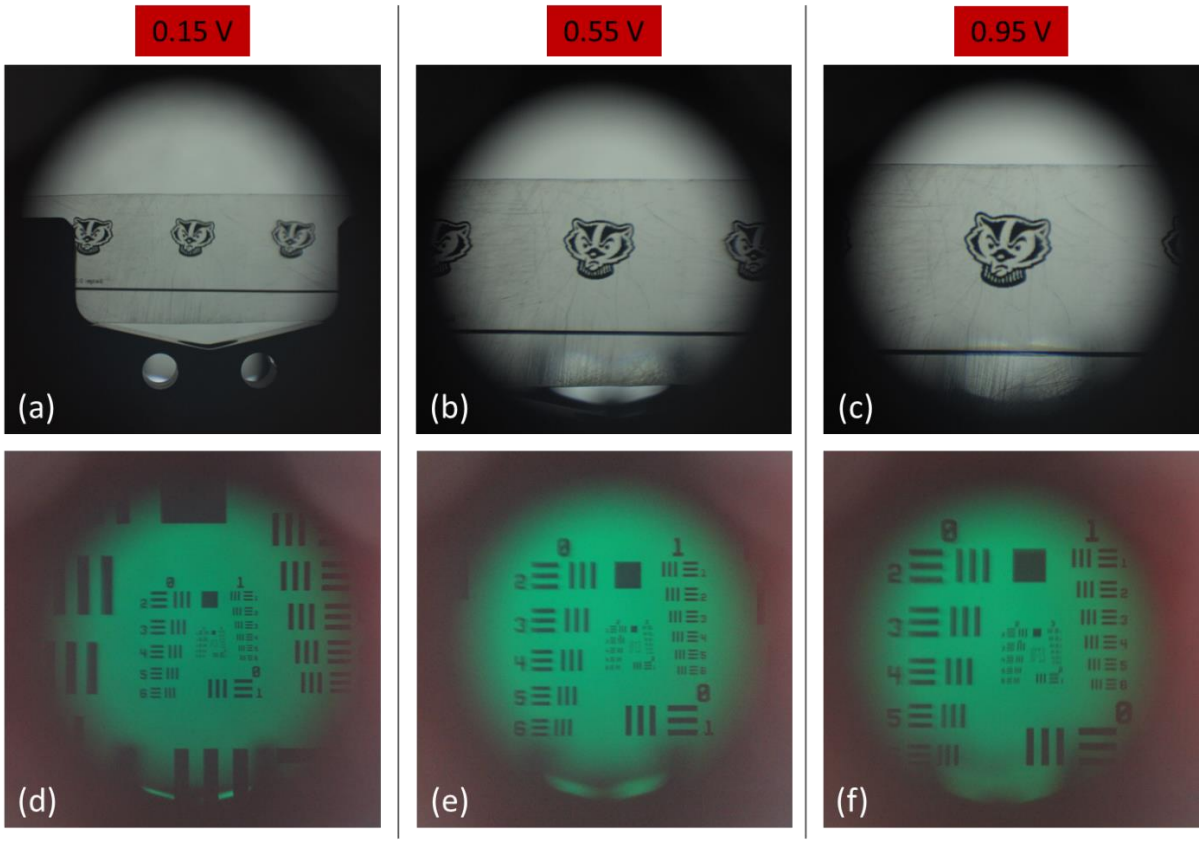

Figure 5.7. *Images from the tunable lens operating in convex regime.* ***(a)-(c)*** *Show the image of a badger, magnifying with increasing applied voltage, and* ***(d)-(f)*** *Show the same trend but with a 1951 USAF resolution target. The resolution was observed to increase along with applied voltage (which corresponds to the focal length and thus f/# of the lens), allowing us to resolve line pairs corresponding to 3.56 lp/mm at 0.15 V, 4.49 lp/mm at 0.55 V, and 7.13 lp/mm at 0.95 V.*

Our imaging set up was then slightly modified to work in the diverging regime of our tunable lens. The manual focus of the DSLR was set to a distance of 240 mm, which placed it on the far side of our tunable lens. Then, when negative voltage was applied to the lens so that it began to diverge, the tunable lens effectively modulates the focal length of the overall system, such that the more voltage applied the farther away the focal point of the system will be shifted (see Figure 5.6b). For each voltage applied to the lens an optical target was moved until best

focus was reached. This was done both with an image of a badger and with a 1951 USAF resolution target. The resulting images can be seen in Figure 5.8. As we would expect for an increasing powerful concave lens, the image of the optical targets shrink as more current is applied to the tunable lens system.

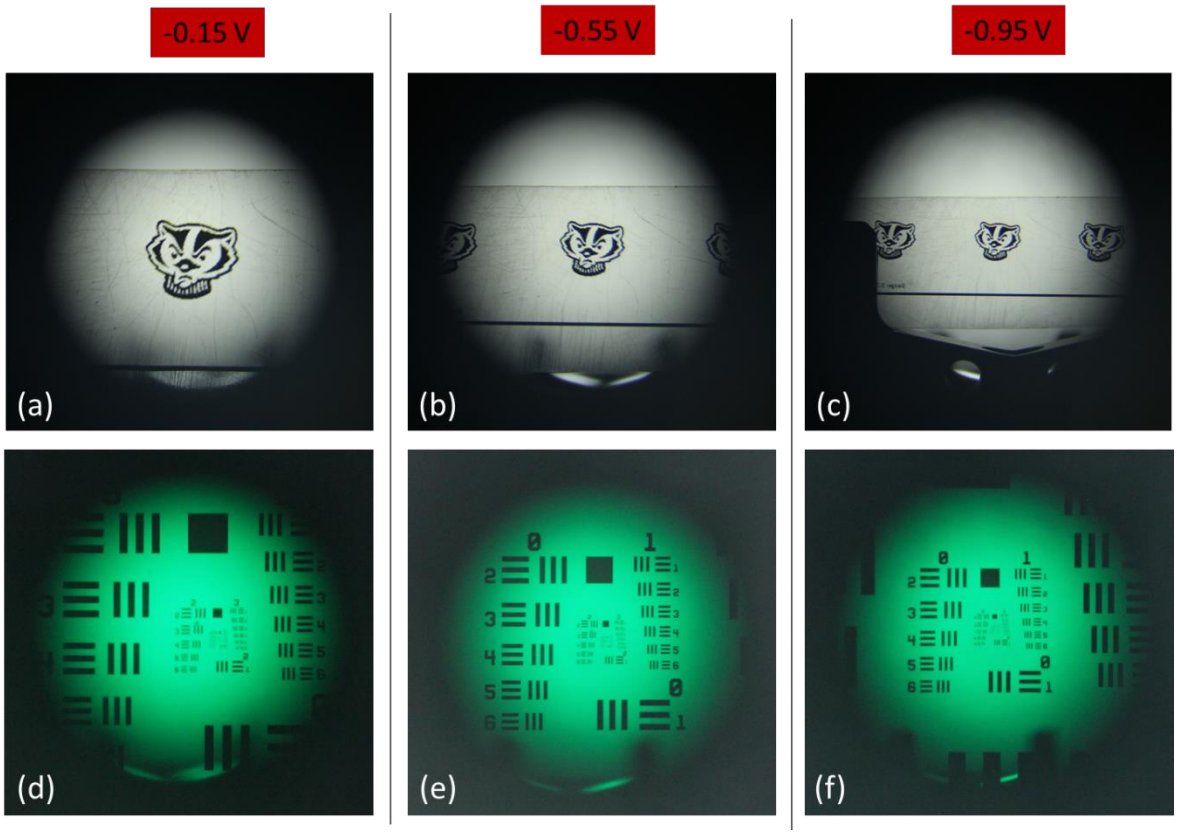

Figure 5.8. *Images from the tunable lens operating in concave regime.* ***(a)-(c)*** *Show the image of a badger, magnifying with increasing applied voltage, and* ***(d)-(f)*** *Show the same trend but with a 1951 USAF resolution target.*

5.6 Discussion

A magnetically actuated liquid lens was developed to function as a focus-tunable lens which operated in both converging and diverging regimes. A winding of copper magnet wire and a NdFeB magnet created a Lorentz force when current was run through the winding, and the

resulting displacement of liquid corresponded to a change in focal length of our lens, either concave of convex depending on the direction of current. We characterized the range of focal lengths achievable by the lens, observing smooth, asymptotic curves for both regimes of operation.

We also measured and characterized the wavefront produced by the lens as it actuates using a Shack-Hartmann wavefront sensor. The resulting data was fit with Zernike polynomials, the coefficients of which are reported in this report. We observed very low spherical aberration, and the most significant contributor to aberrations was observed to be astigmatism, which may be from defects in the lens housing, or defects introduced during the fabrication process. Overall, aberrations were small, indicating a good lens quality. Finally, we imaged utilized a DSLR camera to take images with the lens to observe focal length tuning, and to measure the resolution of the lens, which was found to be 7.13 lp/mm.

References

[1] Yu, H.; Zhou, G.; Chau, F.S.; Sinha, S.K. Tunable electromagnetically actuated liquid-filled lens. *Sensors Actuators, A Phys.* **2011**, *167*, 602–607.

[2] Lee, S.W.; Lee, S.S. Focal tunable liquid lens integrated with an electromagnetic actuator. *Appl. Phys. Lett.* **2007**, *90*, 2005–2008.

[3] Oh, S.H.; Rhee, K.; Chung, S.K. Electromagnetically driven liquid lens. *Sensors Actuators, A Phys.* **2016**, *240*, 153–159.

[4] Liu, C.S.; Lin, P.D.; Lin, P.H.; Ke, S.S.; Chang, Y.H.; Horng, J. Bin Design and characterization of miniature auto-focusing voice coil motor actuator for cell phone camera applications. *IEEE Trans. Magn.* **2009**, *45*, 155–159.

[5] Kim, M.; Kim, H.; Gweon, D.G. Design and optimization of voice coil actuator for six degree of freedom active vibration isolation system using Halbach magnet array. *Rev. Sci. Instrum.* **2012**, *83*.

[6] Liu, C.-S.; Lin, P.D. Miniaturized auto-focusing VCM actuator with zero holding current. *Opt. Express* **2009**, *17*, 9754.

6. Summary and Future Work

We have developed and demonstrated focus-tunable liquid lenses of two different actuation mechanisms—EWOD actuation and magnetic actuation. While the two different kinds of lenses were done much different scales relative to their overall size, together they serve as a good example of what tunable lenses and tunable lens imaging systems are capable of. Our electrowetting microlens array shows what a novel form factor imaging system might look like in the future, and its high levels of reconfigurability leaves open many options including extremely wide FOV imaging (up to 360°) and even in future applications 3D imaging. Our magnetically actuated lens showed a very large focal length range in a robust design.

Future work on the flexible array should include further refinement of the fabrication process in order to verify consistency and reproducibility of lens quality as measured by resolution and Zernike coefficients. This would involve more detailed measurements of the resolution of both individual lenses and of the system as a whole. Other valuable characterizations of the lens would involve assessing the degree of chromatic aberration and making experimental measurements of response times and focal length repeatability of the lens. Additionally, we might dive into further exploration of different configurations of the flexible array, such as on a concave surface to explore its 3D imaging capabilities. Utilizing the array to imagine scenes with greater depth of field should also be explored, since the independent tunability of the focal length of each lens in the array will allow us to capture images from multiple focal planes simultaneously.

Further work to transform the microlens array into a fully integrated microcamera area is also a goal for this system. Developing or finding sensors of suitable quality and integrating them into the same sheet as the microlenses would fully consolidate the aim of this work. Such a fully

integrated array would need to also show increased longevity of the electrowetting microlenses. In particular, future might look even deeper into available nanocoating technologies to achieve and sustain desired surface properties and ensure materials used are fully impermeable to the liquids which compose the lens.

Future work on the magnetically actuated array might involve attempts to scale-down the device in order to make it more robust in the face of vibration and gravity. Work will also need to be done in regards to the choice of membrane and liquids used by the device so that the optical clarity of the lens can be maintained over long periods of time.

APPENDIX

Recipes used in fabrication processes described in the preceding chapters can be found here. They have been divided into broach categories to help structure this appendix.

A1. Photoresist recipes

All recipes utilized a Karl Suss MA6 mask aligner set to soft contact and powered at 10 mW/cm^2 for exposure steps, and all baking steps were performed on hot plates unless otherwise noted.

1. Su-8 2150

Su-8 2150, an extremely thick (several hundred microns) negative photoresist from MicroChem Corp. (Westborough, MA, USA). The thickness of the film means that there is very high levels of strain (especially with a light-field mask) which this recipe has been designed to combat.

- Prepare substrate with thorough cleaning and oven bake for dehydration, then spin coat either Omnicoat or a layer of Su-8 2000.1 to improve adhesion. Both should be followed by a bake step.
- Spin coat Su-8 2150 first at 500 rpm for 30s, then ramp up to 1800 rpm for 45 s (yields a nominal thickness of ~250um)
- Manually remove edge bead with angled razor blade and clean wafer backside with acetone soaked cleanroom wipe
- Soft bake by placing on a room temperature hot plate which is then ramped to 65°C at a rate of 300°C/hr then holding at 65°C for 15 minutes before ramping to

95°C (rate of 300°C/hr) and hold at 95°C for 5 hr. After 5 hr hot plate should be turned off and allowed to return to room temperature with wafer still on it.

- Expose for 15.5 s six times (x6) with a 120 s wait time between each exposure.
- Allow wafer to rest for 30 minutes
- Post exposure bake by ramping hot plate from room temp to 55°C at rate of 300°C/hr, then hold at 55°C for 5 hr. After 5 hr hot plate should be turned off and allowed to return to room temperature with wafer still on it.
- Develop in Su-8 developer for 17 minutes with gentle agitation. Wafer if not fully developed until removing it from the developer and squirting it with IPA no longer produces a milky-white liquid.

2. S1813

S1813 also known as Shipley 1813, a positive photoresist from MicroChem Corp. (Westborough, MA, USA)

- For ~1.9 μm thickness, spin coat at 2500 rpm for 30 s.
- For ~2.4 μm thickness, spin coat at 1500 rpm for 30 s.
- Soft bake at 115°C for 60 s.
- Expose for 9.5 s, or when working on sensitive thin films (i.e. thin coatings of Parylene or CYTOP) utilize multiple exposures while mask remains on contact with wafer. In this case, expose for 2.4 s four times (x4) with a 120 s wait time between each exposure.
- Develop in MF-321 for 90 s.
- Optional hard bake at 115°C for 2 min.

3. S1827

S1827 also known as Shipley 1827, a positive photoresist from MicroChem Corp. (Westborough, MA, USA)

- For ~4 μm thickness, spin coat at 2500 rpm for 30 s.
- Soft bake at 115°C for 2 min.
- Expose for 20 s, or when working on sensitive thin films (i.e. thin coatings of Parylene or CYTOP) utilize multiple exposures while mask remains on contact with wafer. In this case, expose for 2.5 s eight times (x8) with a 120 s wait time between each exposure.
- Develop in MF-321 for 90 s.
- Optional hard bake at 115°C for 2 min.

4. KL 1604

KL 1604, a negative lift-off resist from KemLab, Inc., (Woburn, MA, USA)

- Spin coat at 1500 rpm for 30 s.
- Use a swab dipped in acetone to do a manual edge bead removal from the waver
- Soft bake at 110°C for 60 s.
- Expose for 7.2 s, or when working on sensitive thin films (i.e. thin coatings of Parylene or CYTOP) utilize multiple exposures while mask remains on contact with wafer. In this case, expose for 2.4 s three times (x3) with a 120 s wait time between each exposure.
- Post exposure bake at 110°C for 60 s.
- Develop in MF CD-26 for 60s.

- Do not hard bake.

A2. Parylene recipes

The following recipes were developed for the LabTop 3000 Parylene coater (Para Tech Coating, Inc., Aliso Viejo, CA). A Parylene film is formed at ambient temperatures by utilizing a vapor deposition polymerization (a form of CVD) under vacuum. This process involves three main steps. First, vaporization, where the raw material to the system, a Parylene dimer, sublimates under pressure and low heat. Second, pyrolysis, where the Parylene dimer is broken into a monomer via extreme heat. Third, deposition, where the monomer redeposits on the substrate/chamber to form a fully conformal polymer film.

1. ***Parylene C***

   Parylene C is a well-known and widely-used form of Parylene, so named because the benzene ring which forms the basis of the Parylene monomer substitutes a chlorine atom attached for one aromatic hydrogen.

   - Load substrates (wafers) into the deposition chamber, placing them as radially equidistance from the center of the chamber as possible. Wafers should be placed on the lowest possible racks in the chamber the maximize film thickness (Parylene C will deposit at higher rates towards the bottom of the chamber then towards the top because Parylene C is more likely to redeposit at higher temperatures. Since the bottom of the deposition chamber is closer to the pyrolysis zone of the Parylene coater and the top of the deposition chamber is closer to the liquid nitrogen cold trap, the bottom of the deposition chamber will have a higher ambient temperature).

- Load Parylene dimer in aluminum foil boat into vaporization chamber. The following recipe will for a range of C dimer masses (from 0.75g to 7g). 2.0 g of Parylene C dimer results in a film thickness of ~2.2 μm. 2.5 g of Parylene C dimer results in a film thickness of ~2.752 μm. 3.97 g of Parylene C dimer results in a film thickness of ~ 3.75 μm.
- Seal Parylene coater and pump down to vacuum levels of at least 25 Mic
- While waiting, program the Parylene coater with the following recipe
    - Pyrolysis temperature: 650°C
    - Post-pyrolysis temperature: 220°C
    - Vaporizer temperature profile:

Ramp	Temperature	Soak
5 min	130°C	10 min
5 min	140°C	10 min
5 min	150°C	10 min
5 min	160°C	10 min

- Add liquid nitrogen to the cold finger until full, top off cold finger with more liquid nitrogen every 30 minutes until deposition in complete
- Wait for vacuum levels to drop below 15 Mic
- Turn on pyrolysis and post-pyrolysis heaters and wait (approximately 30 min) for both to reach and stabilize at set temperature
- Start vaporization program and turn on rotational drive
- Once program is complete, turn off pyrolysis and post-pyrolysis heaters and wait until the pyrolysis zone cools to a temperature of 100°C or lower
- Vent system, remove wafers, and preform thorough cleaning of chamber

2. Parylene AF4

Parylene AF4 rare form of Parylene, so named because the alpha hydrogen atoms of the molecule are replaced with fluorine. This gives Parylene AF4 a number of attractive features, including superior penetration depths and film qualities, increased durability in the face high temperatures and UV exposure, and increased hydrophobicity. Parylene AF4 requires higher pyrolysis temperatures to break the dimer into a monomer.

- Before beginning AF4 deposition, the Parylene coater must be thoroughly and extensively clean, especially if previous depositions were of a different kind of dimer (i.e. Parylene C). First, a cleaning cycle should be run to burn off any residual non-AF4 Parylene dimer from the vaporization chamber, then the program outlined below should be run at least once on an empty chamber (i.e. no dimer, no samples).
- Wrap outside of liquid nitrogen cold finger (where excess dimer will deposit) in a cleanroom wipe that has been folded in half. Secure in place using copper wire. This will help prevent post-deposition ‘explosions’ of excess Parylene fragments off the cold finger, which can severely contaminate newly-deposited films.
- Load substrates (wafers) into the deposition chamber, placing them as radially equidistance from the center of the chamber as possible. Wafers should be placed on the highest possible racks in the chamber the maximize film thickness (Parylene AF4 will deposit at higher rates towards the top of the chamber then towards the bottom because Parylene AF4 is more likely to redeposit at lower temperatures. Since the bottom of the deposition chamber is closer to the

pyrolysis zone of the Parylene coater and the top of the deposition chamber is closer to the liquid nitrogen cold trap, the top of the deposition chamber will have a lower ambient temperature).

- Load Parylene dimer in aluminum foil boat into vaporization chamber. The following recipe will for a range of AF4 dimer masses (from 1.0 g to 4.1 g) with only slight modifications (which will be noted below). 2.21 g of Parylene AF4 dimer results in a film thickness of ~425 nm. 4.1 g of Parylene AF4 dimer results in a film thickness of ~800 nm.
- Seal Parylene coater and pump down to vacuum levels of at least 25 Mic
- While waiting, program the Parylene coater with the following recipe
    - Pyrolysis temperature: 705°C (note: white specks visible on the deposited AF4 film indicate that not all of the dimer has been cracked to the monomer. In this event, pyrolysis temperature must be increased).
    - Post-pyrolysis temperature: 25°C (OFF)
    - Vaporizer temperature profile:

Ramp	Temperature	Soak
5 min	130°C	10 min
5 min	135°C	40 min
3 min	140°C	5 min
2 min	145°C	5 min

Note: duration of 135°C soak will be dependent on amount of dimer. For dimer of mass less then 4.1g, a shorter soak will be sufficient.

Vaporization temperature should be held at 135°C until no more dimer appears to be being deposited (i.e. no more color change on a Silicon dummy wafer).

- Add liquid nitrogen to the cold finger until full, top off cold finger with more liquid nitrogen every 30 minutes until deposition is complete, and continue to fill until ~45 minutes prior to expected venting time (keeping the finger cold also helps prevent any potental 'explosions' off finger that redeposit excess Parylene on samples).
- Wait for vacuum levels to drop below 15 Mic
- Turn on pyrolysis heater (post-pyrolysis heater should be OFF) and wait (approximately 30 min) for the heater to reach and stabilize at set temperature
- Start vaporization program and turn on rotational drive
- Once program is complete, turn off pyrolysis heaters and wait until the pyrolysis zone cools to a temperature of 100°C or lower
- Vent system, remove wafers, and perform thorough cleaning of chamber

A3. Plasma recipes

This section contains recipes for plasma-based cleanroom steps, including both plasma-aided depositions (i.e. RF and DC sputtering utilizing CVC sputterer) and plasma etching (RIE utilizing Plasma-Therm 790).

1. ***Copper deposition via magnetron sputtering***

   Results in a ~275 nm Cu film:

   - Power: 200 W (DC)
   - Gas flow: 26 sccm argon
   - Pressure: 10 mTorr
   - Ramp time: 5 minutes
   - Deposition time: 30 minutes

- Continuous (full) rotation, speed 5.

2. ***SiO2 deposition via RF sputtering***

   Results in ~81 nm protective chimney around cathode and ~125 nm without chimney:

   - Power: 140 W (RF)
   - Gas flow: 26 sccm argon
   - Pressure: 10 mTorr
   - Ramp: 10W/min (up and down)
   - Pre-sputter (shutter closed): 3 min
   - Deposition time: 2.5 hr
   - Continuous (full) rotation, speed 4.

3. ***CYTOP etching via RIE***

   Etch rate of ~8.33 nm / s:

   - Power: 200 W
   - Gas flow: Oxygen- 50 sccm
   - Pressure: 75 mTorr

4. ***Parylene C etching via RIE***

   Etch rate of ~6 nm / s:

   - Power: 400 W
   - Gas flow: Oxygen- 100 sccm
   - Pressure: 200 mTorr

5. ***Parylene AF4 etching via RIE***

   Etch rater of 5 nm / s

   - Power 200 W

- Gas flow: Oxygen- 80 sccm
- Pressure: 150 mTorr

A4. Liquid lens well fabrication recipe

The well which was used to contain the liquids of our focus tunable lenses took many forms before reaching the design ultimately used in Chapter 4. Ideally, we desire a flexible but hydrophilic material, but such materials are in short supply, and hydrophilicity is not a strict requirement. This is why early versions of this well/ring were fabricated by molding PDMS (see section 3.3). However, the hydrophilic surfaces of our flexible sheet are highly sensitive to contamination that destroy their hydrophilicity—PDMS and other silicone rubbers among them. This sensitivity also extended to applications of any kind of epoxy to the surface.

We therefore perused non-chemical adhesives, and settled on hot glue (a mixture of 50% ethylene vinyl acetate copolymer and 50% petroleum resin and 50%). The hot glue was measured by volume and then placed in a flat-bottom PTFE dish. This dish was placed in an oven at 140°C for several hours until it had melted to form a flat sheet. It was then allowed to cool (and reharden) before the sheet was removed from the PTFE dish. After this steel punches of two different diameters were used to cut the sheet into rings.

To adhere the rings to our flexible lens sheet they were carefully placed around each electrode center for our lenses. A 3 inch wafer was placed on top of the rings to weigh them down and small weights were also dispersed over the wafer to ensure that the bottom of the rings made good contact with the flexible sheet. The whole set up was then transferred to a hotplate set at 90°C for about four minutes (or as long as it takes for the bottom layer of the hot glue rings to just soften enough to adhere to the flexible sheet). At this point the flexible sheet should

immediately be removed from the hot plate and allowed to cool back to room temperature. Once it is fully cooled and the hot glue has fully set the spare wafer and weights can be removed.

A similar technique can also be used to seal the cover slip (PET or glass) the liquid chamber in place to ensure that there is no evaporation of the liquids. In this case small weights (5-10g) should be pre-heated on a 100°C hot plate or in an oven. The lens should be filled with its liquids and then the cover slip laid over the top of the ring, taking care to ensure that there is no air in the chamber. The heated weight can then be transferred to rest of the top of the cover slip for less then five seconds before being lifted away. The liquid lens is now fully sealed.